Journal of Materials Chemistry C

PAPER

View Article Online
View Journal | View Issue

Cite this: J. Mater. Chem. C, 2016, 4, 3798

Synthesis and optoelectronic properties of chemically modified bi-fluorenylidenes†

Mateusz Wielopolski,[a] Magdalena Marszalek,[b] Fulvio G. Brunetti,[c] Damien Joly,[c] Joaquín Calbo,[d] Juan Aragó,[d] Jacques-E. Moser,[a] Robin Humphry-Baker,[b] Shaik M. Zakeeruddin,[b] Juan Luis Delgado,*[ef] Michael Grätzel,*[b] Enrique Ortí*[d] and Nazario Martín*[cg]

Received 26th October 2015,
Accepted 8th December 2015

DOI: 10.1039/c5tc03501e

www.rsc.org/MaterialsC

The development of new light harvesting materials is a key issue for the progress of the research on organic & hybrid photovoltaics. Here, we report a new class of organic sensitizers based on the bi-fluorenylidene moiety as π-linker within the donor–π-linker–acceptor (D–π–A) scheme. The new dyes are endowed with electron donor and electron acceptor units at strategic positions in order to improve their electronic and light-harvesting properties. The comprehensive study of these compounds through the use of different experimental and theoretical techniques, provides an in-depth understanding of their electronic and photophysical properties, and reveal their interest as photovoltaic materials.

Introduction

Within the field of renewable energies, solar energy is expected to play a prominent role. The search for new materials able to efficiently convert solar energy into electrical power is a current challenge for materials scientists.[1] The utilization of light-harvesting materials would bring new advantages such as the possibility of processing directly from solution, affording lighter and cheaper flexible solar devices.

Dye-sensitized solar cells (DSSCs) based on organic dyes adsorbed on TiO_2 semiconductor electrodes emerged as a new generation of sustainable photovoltaic devices.[2] Their attraction to chemists, physicists and engineers originates not only from the already established high incident-photon-to-current conversion efficiencies and low-cost production but also from the scientific interest in their operational principles.[3] The fabrication of high-performance DSSCs requires the development of efficient organic dyes, whose molecular structures are optimized to provide sufficient light-harvesting features, good electronic communication between the dye and the conduction or valence band of the semiconductor, and a controlled molecular orientation on the semiconductor surface.[4]

Due to the almost infinite synthetic versatility and the high potential in molecular design, precise control of the photophysical and electrochemical properties may be achieved by the modification of the chromophore skeleton or the introduction of substituents.[5] Hence, a whole arsenal of molecular structures of organic dye sensitizers for DSSCs is present in the literature, and the information about the relationship between the chemical structure of the dyes and their photovoltaic performances in DSSCs is steadily increasing. In fact, families of organic dyes, which exhibit high DSSC performances, such as polyenes, hemicyanines, thiophene-based dyes, coumarins, indolines, heteropolycyclic dyes, boron dipyrromethenes (BODIPYs), merocyanines, xanthenes, perylenes, carbazoles, porphyrins, catechols, polymeric dyes, squaraines, cyanines and phthalocyanines (Pcs) have been reported.[6] In our group we have also designed exTTF- and hemiexTTF-based materials, where exTTF stands for 9,10-di(1,3-dithiol-2-ylidene)-9,10-dihydroanthracene, bearing cyanoacrylic acid or rhodanine as the accepting fragment.[7] This structural versatility illustrates the scientific interest and progress in the quest for new molecular architectures to be used as sensitizers in DSSCs.

According to the above mentioned reports on organic dyes, requirements such as the presence of an anchoring group,

[a] Photochemical Dynamics Group, Institute of Chemical Sciences and Engineering, Ecole Polytechnique Fédérale de Lausanne, CH-1015 Lausanne, Switzerland
[b] Laboratory for Photonics and Interfaces, Institute of Chemical Sciences and Engineering, Swiss Federal Institute of Technology, CH-1015 Lausanne, Switzerland. E-mail: michael.graetzel@epfl.ch
[c] IMDEA-Nanoscience, Ciudad Universitaria de Cantoblanco, 28049 Madrid, Spain
[d] Instituto de Ciencia Molecular, Universidad de Valencia, 46980 Paterna, Spain. E-mail: enrique.orti@uv.es
[e] POLYMAT, University of the Basque Country UPV/EHU, Avenida de Tolosa 72, 20018 Donostia-San Sebastian, Spain. E-mail: juanluis.delgado@polymat.eu
[f] Ikerbasque, Basque Foundation for Science, 48011 Bilbao, Spain
[g] Departamento de Química Orgánica, Facultad de Ciencias Químicas, Universidad Complutense de Madrid, 28040 Madrid, Spain. E-mail: nazmar@quim.ucm.es

† Electronic supplementary information (ESI) available: Synthesis and characterization of all the dyes (Fig. S1–S41). B3LYP/cc-pVDZ optimized geometries (Fig. S42), representation of the HOMOs and LUMOs (Fig. S43) and spin-density distributions of the cations (Fig. S44). Lowest-energy excited states calculated for neutral and cationic dyes (Tables S1 and S2). Differential absorption spectra (Fig. S45 and S46). Photovoltaic measurements (Fig. S47 and Table S3). See DOI: 10.1039/c5tc03501e

efficient coupling to the conduction band of TiO_2 and high molar absorption coefficients can be fulfilled by chemical modification of the dye structure through the introduction of electron-donating and -accepting groups and by expansion of π-conjugation. Assuring directional transport of electrons and chemical stability, and preventing dye aggregation, on the other hand, is achieved through the introduction of sterically hindering substituents such as hydrophobic long alkyl chains and aromatic units onto the chromophore skeleton.[5d] In summary, to obtain new and efficient organic dye sensitizers for DSSCs, novel molecular designs capable of controlling not only the photophysical and electrochemical properties of the dyes themselves but also their molecular orientation and arrangement on the TiO_2 surface are necessary.[8]

Herein, we present a new class of organic sensitizers based on fluorene and bi-fluorenylidene as π-linkers within the donor–π-linker–acceptor (D–π–A) scheme. DSSCs based on 2-donor, 7-acceptor, 9-alkyl chain fluorenes have been extensively studied.[9] However, bi-fluorenylidenes have been comparatively less studied. Bi-fluorenylidenes and their thiophene-based analogues have been used as electron acceptors[10] or as monomers to prepare low bandgap polymers.[11] In this work, we have carried out a systematic study on the synthesis of a variety of fluorene derivatives, such as 2,7-donor, 9-acceptor and 3,6-donor, 9-acceptor fluorenes. Furthermore, we have also prepared a series of suitably functionalized bi-fluorenylidenes endowed with electron-donor and electron-acceptor units at strategic positions. In particular, this work aims to establish the relationship between precise and controlled changes of the molecular architecture and their impact on the electronic structure of the dyes. Photophysical and theoretical studies provide in-depth insights into the effects of electronic structure modification on the charge transfer between the dyes and TiO_2. All investigated molecules are shown in Chart 1. **F2a**, **F3a** and **F3b** are mono-fluorene dyes with two diphenylamine (DPA) donor units linked to the phenyl rings of the fluorene moiety and a cyanoacrylic acid (CA) group as the acceptor. For the connection of the DPAs, different linkage patterns have been applied. Taking **F1** as the mono-fluorene reference structure, the donor units in **F2a** and **F3a** are linked in *meta* and *para* positions, respectively. Compared with **F3a**, **F3b** presents a conjugated phenylenevinylene spacer connecting the DPA units to the fluorene core. On the other hand, **BF1**, **BF3a**, **BF3b** and **BF3c** consist of a bi-fluorenylidene core and a carboxylic acid (COOH) accepting unit. **BF3a** and **BF3b** contain DPA donors attached *via* the same π-conjugated linkers as in **F3a** and **F3b**, respectively, and **BF1** and **BF3c** lack of an explicit donor part and constitute reference compounds. The investigation focuses on the charge transfer properties and their dependence on parameters such as (i) the variation of the anchoring moieties: CA *vs.* COOH, (ii) the change in the distance and the π-conjugated linker between the donor and the anchoring/acceptor groups and (iii) the difference in the conjugation pattern between *meta* and *para* substitution. Thus, we explore the effects of specific structural modifications on the electronic, photophysical, and photovoltaic features of the dyes.

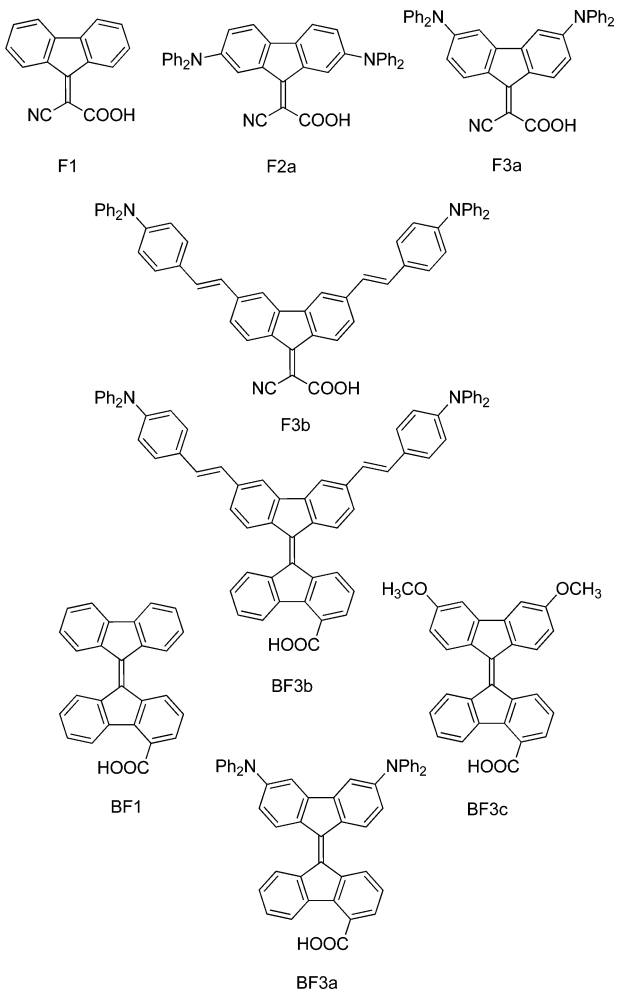

Chart 1 Chemical structure of the dye molecules.

Experimental section

Absorption spectra (Cary 5, Varian), fluorescence spectra (Fluorolog 3, Horiba) and NMR spectra (AVANCE-400, Bruker) were recorded with the indicated instruments.

Differential pulse voltammetry (DPV) measurements

The measurements were conducted using an Autolab system (PGSTAT30, Metrohm, Switzerland). A typical, three-electrode setup consisting of a glassy carbon electrode (working electrode), a Pt plate (auxiliary electrode) and a Pt wire (quasi-reference electrode) was used along with the ferrocene/ferrocenium redox couple as an internal standard. The concentration of the dye in dichloromethane solvent was 0.1 mM and 0.1 M $TBAPF_6$ was added to improve the conductivity. Differential pulse voltammetry was performed in order to enable precise determination of the oxidation potentials.

Computational methods

The molecular geometry of the dyes was fully optimized *in vacuo* and in dichloromethane solution using density functional theory (DFT) calculations with the B3LYP[12] functional and the cc-pVDZ[13] basis set as implemented in the Gaussian 09

(version C.01)[14] program package. The radical cation species were obtained by fully relaxing the optimized geometries of the neutral dyes with a charge of +1 assuming a doublet spin configuration. Ionization potentials were calculated as the adiabatic energy difference between the fully-relaxed cationic and neutral species in their respective doublet and singlet electronic ground state. Spin densities were computed to predict the localization of the unpaired electron in the cationic species. Time-dependent DFT (TD-DFT)[15] calculations of the lowest-lying singlet/doublet states were performed for all neutral/cation compounds using dimethylformamide (DMF) as solvent. Solvent effects were taken into account using the polarizable continuum model (PCM).[16] Molecular orbitals and spin densities were plotted using Chemcraft 1.6.[17]

Photophysical studies

Time-resolved transient absorption measurements were performed on dye-sensitized, 3 μm-thick, transparent TiO_2 mesoporous films screen-printed on non-conducting microscope slides immersed in dye solutions. The pump–probe technique uses a compact CPA-2001, 1 kHz, Ti:Sapphire-amplified femtosecond laser (Clark-MXR), with a pulse width of about 120 fs and a pulse energy of 1 mJ at a central wavelength of 775 nm. The output beam was split into two parts for pumping a double-stage noncollinear optical parametric amplifier (NOPA) and to produce a white light continuum in a sapphire plate or 387 nm UV light by second harmonic generation of the CPA output in a thin BBO crystal. The NOPA was pumped by 200 μJ pulses at a central wavelength of 775 nm and the excitation wavelength was tuned to 480 nm to generate pulses of approximately 10 μJ. The output pulses of the NOPA were compressed in an SF10-glass prism pair compressor down to duration of less than 60 fs (fwhm). Iris diaphragms were used to decrease the pulse energy down to a few micro joules for the pump and to less than 1 μJ for the probe beam. Transient spectra were measured using a white light continuum (WLC) for probing.

The nanosecond laser flash photolysis employed 7 ns pulses to excite the sample at λ = 480 nm and using a 30 Hz repetition rate. A Powerlite 7030 frequency-doubled Q-switched Nd:YAG laser (Continuum, Santa Clara, California, USA) served as a light source. The laser beam output was expanded by a plano-concave lens to irradiate a large cross-section of the sample, whose surface was kept at a 40° angle to the excitation beam. The laser fluence on the sample was kept at a low level (35 μJ cm^{-2} per pulse) to ensure that, on average, less than one electron is injected per nanocrystalline TiO_2 particle on pulsed irradiation. The probe light, produced by a continuous wave xenon arc lamp, was first passed through a monochromator tuned at different wavelengths to probe a broad spectral range, various optical elements, the sample, and then through a second monochromator, before being detected by a fast photomultiplier tube (Hamamatsu, R9110).

Device fabrication

State-of-the-art double-layer mesoporous TiO_2 layer (8 μm of 20 nm particle (DSL 18NR-T, DYESOL) plus 5 μm of 400 nm light scattering particles (HPW-400NRD, CCIC)) was printed on FTO conducting glass (Solar-4 mm, Nippon Sheet Glass Co, Ltd). The double-layer TiO_2 film was sensitized by immersing it into a THF/EtOH (1 : 4) solution of the respective dye (0.3 mM) for 15 h at room temperature. The composition of the electrolyte was 1.0 M 1,3-di-methylimidazolium iodide, 30 mM I_2, 0.5 M *tert*-butylpyridine, 0.1 M lithium iodide and 0.1 M guanidinium thiocyanate in a mixture of acetonitrile and valeronitrile (85/15, v/v). A platinized FTO conducting glass (LOF TECH 7, Pilkington) was used as counter electrode. The spectral distribution of the light source simulates the AM 1.5G solar irradiation characteristics (Xe 450W/K113, filter) with a spectral mismatch of less than 4%. The exposed area of the devices was 0.16 cm^2, a black tape mask being used to exclude any stray light. An antireflection film (ARCTOP, Mihama Co.) was attached on the photoanode side.

Results and discussion

Synthesis

New dyes based on different fluorene substitution patterns, such as 2,7-donor, 9-acceptor and 3,6-donor, 9-acceptor fluorenes or even bi-fluorenylidene units, have been carefully designed.

Compounds **F2a**, **F3a** and **F3b** were prepared through a multi-step synthetic route starting with the preparation of fluorenone precursors **1**, **3** and **4**, respectively (see the ESI†). The synthesis of **1**, **3** and **4** was achieved through the Buchwald reaction on the corresponding bromofluorenone precursors. Knoevenagel condensation followed by hydrolysis in the presence of LiOH afforded compounds **F2a**, **F3a** and **F3b** (Scheme 1). The reference compound **F1** was prepared following a previously reported procedure.[18]

In the bi-fluorenylidene (BF) series, esters were obtained using Barton's two-fold coupling between fluorenones **3**, **4** and **9** which were prior converted to fluorenthiones, and 4-carboxymethylester-fluoren-9-tosylhydrazone (**8**) in the presence

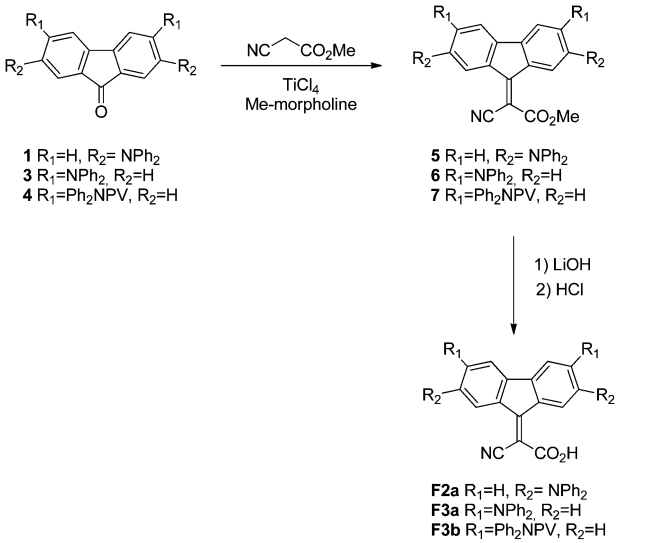

1 R_1=H, R_2= NPh_2
3 R_1=NPh_2, R_2=H
4 R_1=Ph_2NPV, R_2=H

5 R_1=H, R_2= NPh_2
6 R_1=NPh_2, R_2=H
7 R_1=Ph_2NPV, R_2=H

F2a R_1=H, R_2= NPh_2
F3a R_1=NPh_2, R_2=H
F3b R_1=Ph_2NPV, R_2=H

Scheme 1 Synthesis of **F2a**, **F3a** and **F3b**.

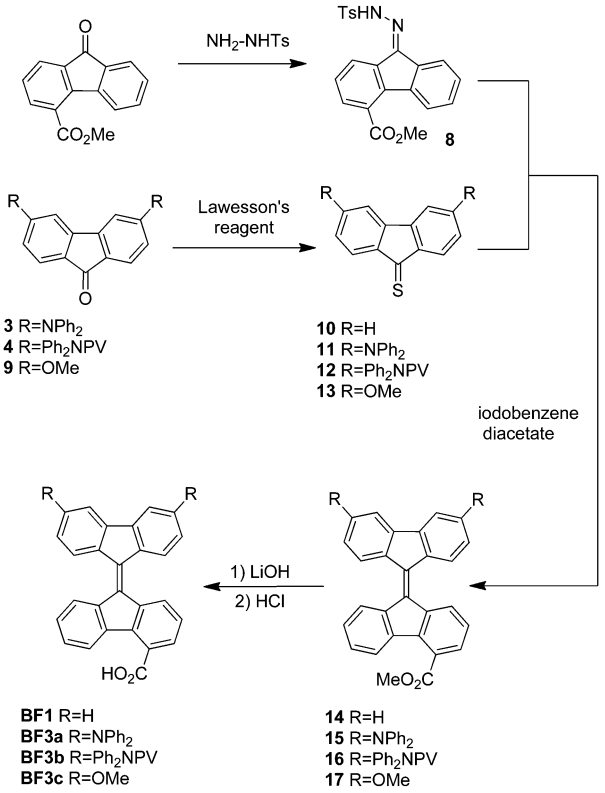

Scheme 2 Synthesis of bi-fluorenylidene derivatives **BF1**, **BF3a**, **BF3b**, and **BF3c**. Compound **10** was synthesized according to an already described procedure.[19]

of iodobenzene diacetate (Scheme 2). The esters were then hydrolyzed to obtain **BF1**, **BF3a**, **BF3b** and **BF3c**.

Redox potentials

Differential pulse voltammetry (DPV) was used to determine the redox potentials of the new synthesized sensitizers. For all the dyes, two oxidation potentials were measured, which are collected in Table 1. The introduction of the DPA units shifts the potentials to less anodic values, the effect being more pronounced when the DPA groups are linked in *meta* (**F2a**) than in *para* (**F3a**) positions. The presence of the second fluorene moiety in **BF3a** and **BF3b** further reduces the oxidation potentials compared to **F3a** and **F3b**, which suggests an effective conjugation between the two fluorene units. **BF3c** presents higher oxidation potentials due to the lower electron-donor character of the methoxy groups when compared with the DPA units.

Table 1 DPV oxidation potentials measured for the fluorene and bi-fluorenylidene dyes in dichloromethane

Dye	$E_{ox,1}$ (V *vs.* NHE)	$E_{ox,2}$ (V *vs.* NHE)
F1	2.05	2.37
F2a	1.45	1.74
F3a	1.59	1.85
F3b	1.59	1.84
BF3a	1.38	1.56
BF3b	1.43	1.74
BF3c	1.72	2.06

Molecular and electronic structure

To analyze the effect of the substitution pattern on the molecular structure, geometry optimizations of the fluorene (**F1**, **F2a**, **F3a** and **F3b**) and bi-fluorenylidene (**BF1**, **BF3a**, **BF3b** and **BF3c**) dyes were performed at the B3LYP/cc-pVDZ level using dichloromethane as solvent. Fig. 1 shows the optimized geometries of **F3a**, **BF3a** and **BF3b** as representative examples (see Fig. S42, ESI† for the geometry of the remaining molecules).

The main difference in the molecular geometry is found when passing from the mono-fluorene to the bi-fluorenylidene derivatives. In the former, the dihedral angle defined by the π-conjugated core and the acceptor moiety through the carbon–carbon double bond is computed close to zero (a maximum dihedral of 7.6° is calculated for **F3a**, Fig. 1). In the bi-fluorenylidene derivatives, the two fluorene units forming the π-conjugated core that separates the donor and acceptor units twist around the central C=C bond to alleviate the steric hindrance between hydrogen atoms in 1 and 8 positions, and form an angle of ~36° (see Fig. 1). The attachment of the donor DPA units in *meta* position determines no significant change in the molecular geometry of **F2a** compared to **F1**. For instance, the C=C bond connecting the fluorene core and the acceptor CA unit has the same length (1.381 Å) for both compounds and the twisting angle around this bond has almost the same value (5.7 and 5.5°, respectively). This is not however the case for compound **F3a**, for which the DPA units are linked in *para* positions. For **F3a**, the exocyclic C=C bond lengthens to 1.395 Å and the twisting angle increases to 7.6°. These changes are due to the larger negative charge borne by the cyanoacrylic unit in **F3a** ($-0.36e$) compared with **F2a** ($-0.25e$) and **F1** ($-0.26e$). The larger charge transfer obtained for **F3a** evidences the more effective electronic communication that takes place between the donor and acceptor moieties when the DPA groups are attached in *para* positions. The extension of the π-conjugated linker in passing from **F3a** to **F3b** reduces the charge transfer and the CA unit in **F3b** is linked by a C=C bond of 1.391 Å and accumulates a net charge of $-0.31e$. The bi-fluorenylidene dyes present very similar geometrical structures due to the larger separation between the donor and acceptor groups and the weaker acceptor character of the COOH group. The only significant difference is the slight lengthening of the central C=C bond linking the two fluorene units in passing from **BF1** (1.386 Å),

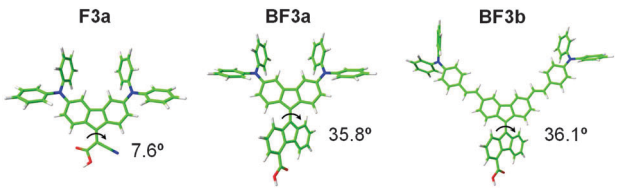

Fig. 1 B3LYP/cc-pVDZ-optimized geometries calculated for **F3a**, **BF3a**, and **BF3b** in dichloromethane. Characteristic dihedral angles are indicated.

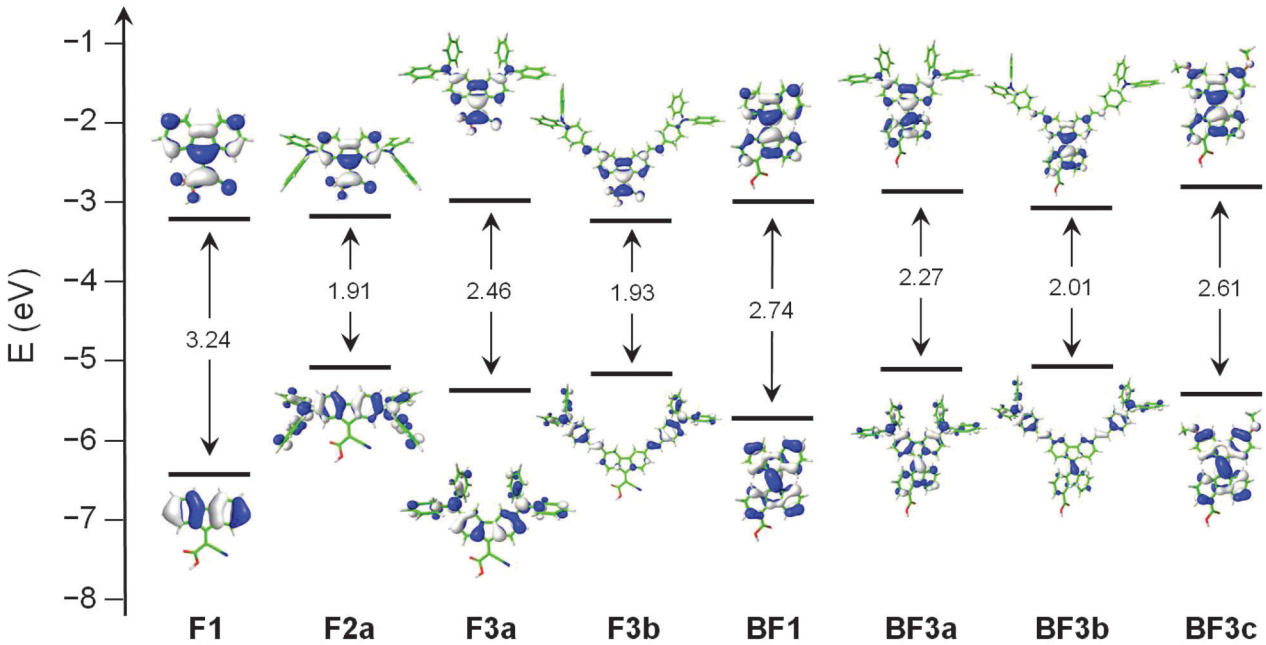

Fig. 2 Energy diagram showing the isovalue contours (±0.03 a.u.) and the relative energies computed for the HOMO and LUMO of all dyes at the B3LYP/cc-pVDZ level in dichloromethane. HOMO–LUMO energy gaps are indicated.

bearing no donor group, to **BF3c** (1.389 Å), **BF3b** (1.391 Å) and **BF3a** (1.392 Å).

The changes introduced in the chemical structure of the dyes strongly influence their electronic and optical properties. The molecular orbital diagram shown in Fig. 2 reveals significant differences between the two families of dyes and among the members of each family. The energies calculated for the highest-occupied (HOMO) and the lowest-unoccupied molecular orbital (LUMO) are collected in Table 2. The HOMO is entirely localized on the fluorene core for **F1**, whereas it spreads over the donor groups and the fluorene core for **F2a** and **F3a**. The attachment of the DPA groups produces a destabilization of the HOMO that is more pronounced for the *meta*-substituted **F2a** (−5.05 eV) than for the *para* isomer **F3a** (−5.35 eV). Compared to **F3a**, the introduction of the phenylenevinylene π-conjugated linkers in **F3b** leads to an additional destabilization of the HOMO (−5.13 eV), which is now mostly located on the DPA units and the linkers. This destabilization stems from the extension of the π-conjugated system.

Table 2 HOMO and LUMO energies (ε), HOMO–LUMO energy gaps (ΔE_{H-L}) and ionization potentials (IP) calculated at the B3LYP/cc-pVDZ level in dichloromethane solution. All data are in eV

Dye	ε_{HOMO}	ε_{LUMO}	ΔE_{H-L}	IP
F1	−6.41	−3.17	3.24	6.33
F2a	−5.05	−3.14	1.91	4.91
F3a	−5.35	−2.90	2.46	5.28
F3b	−5.13	−3.19	1.93	5.06
BF1	−5.68	−2.94	2.74	5.53
BF3a	−5.06	−2.79	2.27	4.90
BF3b	−5.03	−3.02	2.01	4.93
BF3c	−5.36	−2.75	2.61	5.19

The LUMO of the fluorene derivatives remains localized on the acceptor CA moiety and the fluorene core. No significant energy difference between the LUMO of **F1** (−3.17 eV) and **F2a** (−3.14 eV) is predicted, suggesting an inefficient electronic communication between the DPA groups and the fluorene core in **F2a** (Fig. 2). In contrast, the attachment of the DPA units in *para* positions significantly destabilizes the LUMO of **F3a** (−2.90 eV) by 0.27 eV owing to the antibonding interaction of the nitrogen atoms of DPA with the fluorene core (Fig. 2). These trends suggest a more efficient electronic communication between the DPA groups and the fluorene core in **F3a** than in **F2a**. Therefore, as can be seen in Fig. 2 and Table 2, important differences are found in the HOMO–LUMO energy gap (ΔE_{H-L}) depending on the structural changes and the extension of π-conjugation in the mono-fluorene compounds. The most relevant trends are: (i) the attachment of donor DPA groups increases considerably the HOMO energy with small changes in the LUMO energy, (ii) *para* substitution favours the π-conjugation between the DPA units and the fluorene core compared to *meta* substitution and leads to significantly larger HOMO–LUMO gaps (**F2a**: 1.91 eV, **F3a**: 2.46 eV) and (iii) the introduction of phenylenevinylene units as π-conjugated linkers of the DPA units destabilize and stabilize the HOMO and the LUMO, respectively, narrowing the HOMO–LUMO gap (**F3a**: 2.46 eV, **F3b**: 1.93 eV).

Similar conclusions to those extracted for the mono-fluorene systems can be established for the bi-fluorenylidene dyes. For the reference compound **BF1**, the HOMO and LUMO spread over the conjugated bi-fluorenylidene core (Fig. 2), and it presents a narrower HOMO–LUMO gap (2.74 eV) compared with **F1** (3.24 eV) especially due to the destabilization of the HOMO. The introduction of the donor methoxy groups in **BF3c**

raises the HOMO and LUMO energies and slightly reduces the HOMO–LUMO gap (2.61 eV). The same scenario is obtained for **BF3a**, where the substitution of *para* positions with DPA donor fragments increases the molecular orbital energies, especially for the HOMO, leading to a narrower HOMO–LUMO gap of 2.27 eV. The extension of the π-conjugated system in **BF3b** produces an additional narrowing of the HOMO–LUMO gap (2.01 eV) as obtained when comparing **F3a** and **F3b**. However, the changes predicted for the bi-fluorenylidene dyes are somewhat smaller than those found for the mono-fluorene compounds. This is due to the fact that the incorporation of the DPA donor groups does not destabilize the HOMO energy as much as in the mono-fluorene derivatives owing to the spreading of the HOMO over the two fluorene moieties.

It is worth mentioning that the cyanoacrylic acid moiety in all the mono-fluorene dyes (**F1**, **F2a**, **F3a** and **F3b**) remarkably shifts the electronic density of the LUMO onto the anchoring part of the molecule allowing for a more efficient electronic communication with the TiO_2 conduction band compared to the bi-fluorenylidene dyes (**BF1**, **BF3a**, **BF3b**, and **BF3c**) which bear carboxylic acid anchors. The LUMO of the latter actually shows no electron density on the COOH anchoring group (Fig. 2).

Chemical substitution of the dyes has a strong impact on the relative stability of the radical cations obtained upon oxidation. Since these oxidized species are formed just after the electron injection to the semiconductor, they play a key role in the photovoltaic performance of the dyes. Ionization potentials (IPs) were computed as the adiabatic energy difference between the radical cation and the neutral species in their respective ground-state optimized geometries (Table 2), and spin densities were calculated to predict the localization of the unpaired electron in the radical cation species (Fig. S44, ESI†). **F1** shows the most positive ionization potential (6.33 eV), matching the highest oxidation potential found experimentally (2.05 V, Table 1). The introduction of the DPA groups allows for an extra delocalization of the unpaired electron over the donor moieties thus providing more stable cations. In the mono-fluorene series, the lowest IP is obtained for **F2a** (4.91 eV) and the **F3a** cation is predicted to be less stable (IP = 5.28 eV). This trend accords with the experimental oxidation potentials (1.45 and 1.59 V, respectively) and with the higher HOMO energy predicted for **F3a** (Table 2). The extension of the π-conjugated system by the phenylenevinylene linkers adds an extra delocalization for the unpaired electron with the consequent lowering of the IP for **F3b** (5.06 eV) compared to **F3a** (5.28 eV). The bi-fluorenylidene derivatives **BF3a** and **BF3b** exhibit smaller IPs (4.90 and 4.93 eV, respectively) than their mono-fluorene analogues due to the delocalization of the unpaired electron over the second fluorene unit (Fig. S44, ESI†). The presence of the methoxy groups in **BF3c** partially stabilizes the unpaired electron in the cation and reduces the IP (5.19 eV) with respect to **BF1** (5.53 eV). The theoretical picture nicely agrees with the redox potentials experimentally recorded for the fluorene and bi-fluorenylidene series.

Photophysical features

Steady-state absorption. The investigation of the steady-state absorption features of the dyes in solution and after adsorption on TiO_2 films allows for important conclusions on the impact that structural changes have on the electronic properties of the dyes. Furthermore, it is feasible to identify the interactions between the building blocks, *i.e.*, donors, π-linkers and acceptors, when considering the absorptions of the reference structures **F1**, **BF1** and **BF3c**.

Fig. 3 represents the ground-state absorption spectra of all dyes (0.1 mM) in dimethylformamide (DMF) solutions. As seen from the spectrum of **F1**, the mono-fluorene features correspond to a single, broad absorption band between 300 and 400 nm. In **F2a** this absorption is shifted by 40 nm due to the additional interactions with the DPA moieties. Furthermore, the addition of the DPA donors results in the appearance of a broad band in the range between 460 and 650 nm. However, due to the lack of overlap between both maxima we assume only minor electronic communication between the DPA groups and the fluorene core in **F2a**. The situation is completely different when considering the absorptions of **F3a** and **F3b**. In **F3a**, for instance, the substitution of the fluorene unit at the *para* positions leads to a broadening of the spectrum and a significant overlap between all the absorption bands. This implies that, as suggested above based on the geometry and molecular orbital energy differences found theoretically, changing the substitution pattern from *meta* to *para* improves the π-conjugation in comparison to **F2a**. On the other hand, increasing the distance between the DPA and the fluorene core increases the extinction coefficients from 1.5×10^{-4} M^{-1} cm^{-1} in **F3a** to 2.6×10^{-4} M^{-1} cm^{-1} in **F3b** but the broad absorption centered around 422 nm does not undergo a red-shift.

After adsorption to TiO_2 (Fig. 4), a significant blue-shift due to the deprotonation of the anchoring groups is experienced in all dyes. This implies successful binding of all compounds to the TiO_2 surface after 12 h of dye loading.

The bi-fluorenylidene reference compounds **BF1** and **BF3c** exhibit a broad maximum between 400 and 550 nm due to the larger π-electron system of the bi-fluorenylidene core. The maximum in **BF3c** is slightly red-shifted by 12 nm due to the π-extension by the methoxy groups. Both **BF1** and **BF3c**

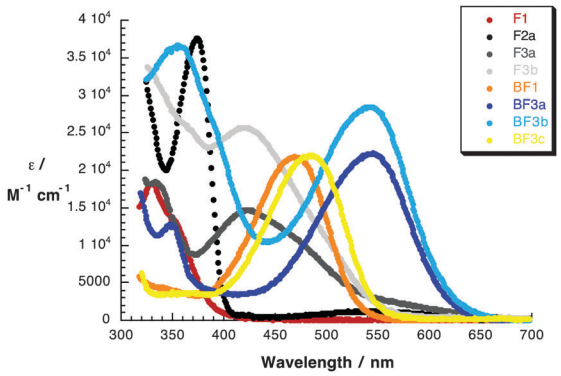

Fig. 3 Steady-state absorption spectra of all investigated dyes in 0.1 mM DMF solutions.

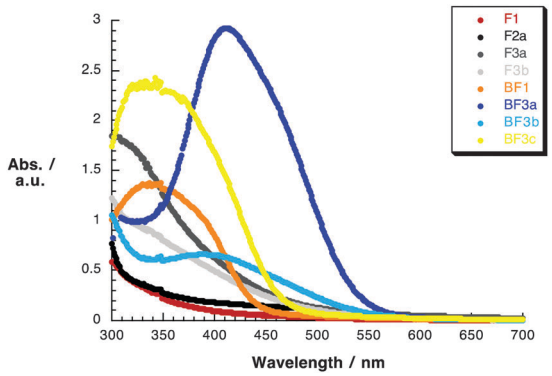

Fig. 4 Steady-state absorption spectra of all investigated dyes adsorbed on 3 μm-thick transparent mesopourous TiO_2 films.

absorb also in the region between 300 and 400 nm with low extinctions. When considering the donor–acceptor dyes **BF3a** and **BF3b**, the broad maxima shift to the red by more than 60 nm due to the remarkable extension of π-conjugation. Furthermore, in the region between 300 and 450 nm a new sharp absorption band arises with extinction coefficients of 1.2×10^{-4} and 3.6×10^{-4} M^{-1} cm^{-1} for **BF3a** and **BF3b**, respectively. The higher extinction in **BF3b** stems once more from the improved delocalization of π-electrons as compared with **BF3a**.

To get more insight into the electronic nature of the experimentally observed absorption bands, theoretical calculations of the lowest-lying singlet excitations ($S_0 \rightarrow S_n$) were performed for all the dyes using the TD-DFT approach and DMF as solvent (Table S1 in the ESI†). For **F1**, the broad band observed around 350 nm originates from the $S_0 \rightarrow S_2$ and $S_0 \rightarrow S_3$ electronic excitations calculated at 357 and 355 nm, respectively. These two excitations are mainly described by one-electron promotions from the HOMO − 1 and HOMO − 2 to the LUMO and involve both the fluorene core and the acceptor CA unit. The lowest-energy $S_0 \rightarrow S_1$ transition computed at 510 nm corresponds to the HOMO → LUMO excitation that implies some charge transfer (CT) from the fluorene moiety, where the HOMO is located, to the acceptor CA unit, where the LUMO mainly resides (Fig. 2). The net charge accumulated by the CA group increases from $-0.26e$ in S_0 to $-0.51e$ in S_1. This CT excitation is not perceivable in the UV-Vis spectrum due to its small computed oscillator strength (f = 0.001) but becomes more evident in the remaining fluorene dyes (Fig. 3 and Table S1, ESI†). For **F2a**, the HOMO → LUMO CT excitation is computed to be more intense (f = 0.036) and is observed in the experiment, and the $S_0 \rightarrow S_4$ and $S_0 \rightarrow S_6$ transitions calculated at 395 (f = 0.606) and 366 nm (f = 0.376), respectively, account for the intense absorption band peaking at 380 nm (Fig. 3). In passing to **F3a**, the features of the absorption spectrum undergone a dramatic change. The variation of the position of the DPA substituents, from *meta* to *para*, induces the appearance of three CT excitations ($S_0 \rightarrow S_1$, $S_0 \rightarrow S_2$, and $S_0 \rightarrow S_3$) calculated at 648, 523 and 437 nm with high oscillator strengths of 0.264, 0.524 and 0.126, respectively (Table S1, ESI†), which account for the intense broad absorption band observed in the 400–640 nm range for **F3a** (Fig. 3). Similar transitions with higher oscillator strengths appear in the same energy region for **F3b** thus explaining the higher intensity of the absorption band observed experimentally (Fig. 3).

For the bi-fluorenylidene **BF1** and **BF3c** dyes, only the $S_0 \rightarrow S_1$ transition contributes to the broad band experimentally observed at around 475 nm (Table S1, ESI† and Fig. 3). This transition is fully described by the HOMO → LUMO monoexcitation located on the bi-fluorenylidene core with some contribution of the oxygen atoms of the additional methoxy groups for **BF3c**. The better optical performance of **BF3a** and **BF3b** associated with the intense broad band observed at 440–640 nm is mainly due to the HOMO → LUMO excitation that implies the bi-fluorenylidene core and the CT from the DPA units to the core, especially for **BF3b** (Table S1, ESI† and Fig. 2). The participation of the phenylenevinylene linkers increases the oscillator strength of the lowest-energy transitions, justifying the higher intensity of the absorption band for **BF3b** (Fig. 3). The anchoring COOH group is not involved in these transitions. The intense band observed for **BF3b** at around 350 nm is due to monoexcitations located on the donor fragment, which are significantly less intense for **BF3a**. $\pi \rightarrow \pi^*$ transitions associated to the bi-fluorenylidene core also contribute to this part of the spectra.

Excited state features

To investigate the charge transfer processes and their kinetics we have employed further spectroscopic investigation methods. Time-resolved transient absorption measurements were performed in order to scrutinize the dynamics of charge injection into TiO_2 and charge recombination between the dyes' oxidized states and the injected electrons.

Femtosecond transient absorption spectra with 480 nm laser excitation were recorded for the donor–acceptor compounds **F2a**, **F3a**, **F3b**, **BF3a** and **BF3b** and the reference compounds **BF1** and **BF3c**. Due to the lack of the electron donating unit only singlet excited-state formation was observed in **BF1** and **BF3c**. The spectral characteristic of the singlet excited state of the bi-fluorenylidene dyes is a broad maximum extending from 520 nm beyond 700 nm (Fig. 5). The formation occurs instantaneously after laser excitation with rate constants of 3.7×10^{12} s^{-1} for **BF1** and 7.8×10^{12} s^{-1} for **BF3c**. Thereby, the singlet excited state signal in **BF1** decays within 50 ps, whereas it is stable on the time scale of our femtosecond experiment for **BF3c** due to the contribution of the oxygen atoms of the additional methoxy groups. The additional donor methoxy groups in **BF3c** add electron density to the molecule, which raises the HOMO–LUMO energies (Fig. 2) and allows for a more stable singlet excited state. The slightly lower HOMO–LUMO energy gap in **BF3c** is also responsible for faster singlet activation as compared with **BF1**. Fig. 5 displays the spectral characteristics of the reference structures as evolved after photoexcitation.

When going to the donor–acceptor dyes **BF3a** and **BF3b** the spectral characteristics are notably different (Fig. S45, ESI†). An instantaneous charge injection into TiO_2 leads to a singlet

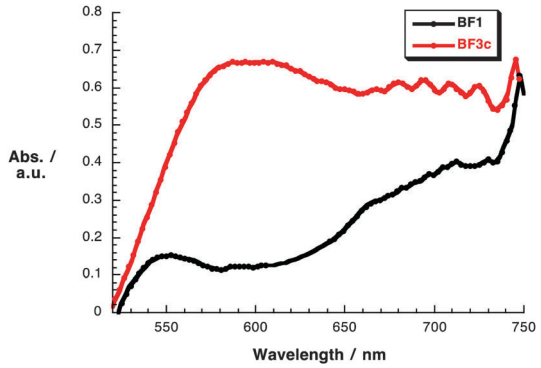

Fig. 5 Differential absorption spectra obtained upon femtosecond flash photolysis (λ_{exc} = 480 nm) of 3 μm-thick TiO_2 films sensitized with **BF1** (black) and **BF3c** (red) with a time delay of 4 ps at room temperature showing the spectral characteristics of the singlet excited states.

bleaching between 500 and 640 nm for **BF3a** and between 500 and 590 nm for **BF3b**. On the other hand, in agreement with the photoinduced absorption studies, a positive signal in the regions beyond 600 nm characterizes the oxidized state of the dyes. Theoretical calculations predict that excitations from the single-occupied molecular orbital (SOMO) and HOMO − 1 to the LUMO, which exhibit a predominant CT nature, contribute the most to the cationic signal of both dyes (Table S2, ESI†). As can be seen from the spectra, the formation of the oxidized state of **BF3a** occurs with a much slower rate constant than for **BF3b**. The charge injection rates differ by one order of magnitude, *i.e.*, 1.5×10^{11} s^{-1} and 6.0×10^{12} s^{-1} for **BF3a** and **BF3b**, respectively. Again, the significantly lower HOMO–LUMO energy gap in **BF3b** is responsible for this trend. Interestingly, the transient absorption spectra of **BF3b** exhibit an isosbestic point. Hence, singlet excited-state energy transfer powers the charge separation between the electron donating DPA and the anchoring group and the subsequent charge injection into TiO_2. The singlet bleaching recovers according to the decay of the signal of the oxidized states. Important in this context is the fact that the charge injection occurs instantaneously with photoexcitation, which proves efficient electronic communication between the electron donating and the anchoring groups. Low-energy singlet excited states facilitate the charge separation and increase the rate for charge injection. Thus, the slower charge injection rate constants measured for **BF3a** point to higher energy singlet excited states, in accord with theoretical predictions (Table S1, ESI†), and justify the lack of the isosbestic point (Fig. S45, ESI†).

Moving on to **F2a** and **F3b**, similar features (singlet bleaching and isosbestic points) due to the formation of the oxidized states of the dyes are found in the corresponding transient absorption spectra (Fig. S46, ESI† – top and middle). However, the smaller size of the π-conjugated system gives rise to higher excitation energies and the spectral features become sharper with their maxima and minima shifted to the blue as compared with the bi-fluorenylidene compounds **BF3a** and **BF3b**. In **F2a** and **F3b** the singlet bleaching is shifted to 530 and 550 nm, respectively, and the broad signature of the oxidized states maximizes at 600 and 660 nm, respectively. Theoretical calculations predict that these signals are assigned to the CT electronic transitions associated with the SOMO → LUMO excitation (Table S2, ESI†). The red-shift of the maxima is well in line with the extension of the π-system in **F3b** as compared with **F2a**. On the contrary, the spectrum of **F3a** (Fig. S46, ESI† – bottom) lacks any excited state features. Considering the more efficient electronic interactions between the DPA and the fluorene in the ground-state in **F3a** (see Fig. 3), we assume that due to the variation of the substitution (*para vs. meta*) the electronic coupling between the donor and the anchoring moiety is altered. Theoretical calculations indeed suggest a better electronic communication between the DPA groups and the CA unit for **F3a**. This is directly correlated with the deactivation kinetics and therefore the charge separation is instantaneously deactivated by an ultrafast charge recombination. As a consequence, charge injection into TiO_2 is hindered and no oxidized state formation is evident in the transient absorption spectrum of **F3a**. This simple change of the position of the substitution on the fluorene moiety goes along with a significant increase of the HOMO–LUMO gap of **F3a** (2.41 eV) as compared with **F2a** (1.90 eV) (Fig. 2).

Considering the charge injection kinetics of **F2a**, **F3b**, **BF3a** and **BF3b** (Table 3), the rates are related to the above-mentioned stabilization of the singlet-excited states, which obviously facilitates the charge injection into TiO_2. An improved stabilization of the singlet-excited state facilitates the formation of the oxidized species of the dyes. Due to the highly delocalized character of the oxidized states the charge injection kinetics may be correlated with the ionization potentials (Table 2),

Table 3 Rate constants for charge injection (k_{CI})/singlet-excited state formation ($k_{Singlet}$), charge recombination without electrolyte (k_{CR}) and dye regeneration with electrolyte (k_{DR}) for all dyes on 3 μm-thick TiO_2 films as obtained by femtosecond transient absorption measurements and nanosecond flash photolysis with 480 nm light excitation

	$k_{CI/Singlet}/s^{-1}$	$k_{CR}/s^{-1}//k_{DR}/s^{-1}$	$\tau_{1/2}$(CI/S)	$\tau_{1/2}$(CR)//$\tau_{1/2}$(DR)
TiO_2 no EL				
F3a$_{Singlet}$	—	—	—	—
F2a	3.0×10^{12}	$1.5 \times 10^{5}//1.8 \times 10^{5}$	0.34 ps	6.49 μs//5.58 μs
F3b	5.0×10^{12}	$2.1 \times 10^{3}//3.7 \times 10^{4}$	0.20 ps	474 μs//27.0 μs
BF1$_{Singlet}$	3.7×10^{12}	—	0.27 ps	—
BF3a	1.5×10^{11}	$3.9 \times 10^{3}//1.1 \times 10^{5}$	6.7 ps	255 μs//8.94 μs
BF3b	6.0×10^{12}	$2.2 \times 10^{3}//1.1 \times 10^{5}$	0.17 ps	454 μs//9.09 μs
BF3c$_{Singlet}$	7.8×10^{12}	—	0.13 ps	—

which in turn explains the fact that that charge injection occurs on equal time-scales as found for the singlet-excited state formation. Proof for this assumption is found by comparing the charge injection rates in **BF3a** and **BF3b** with those for the singlet-excited state formation in **BF1** and **BF3c**. Therefore, it can be safely assumed that the photoexcitation of the donor–acceptor dyes results in an instantaneous formation of the oxidized state and an immediate charge injection into TiO_2 due to very efficient π-conjugation of the molecules.

Apart from a rapid charge injection, a slow charge recombination is crucial for an effective performance of the dyes in photovoltaic devices. To probe the dynamics of the regeneration of the oxidized states of the dyes in the presence and in the absence of a redox electrolyte environment complementary nanosecond flash photolysis experiments have been employed.

In the absence of the redox electrolyte the regeneration of the dyes' ground state occurs by back-electron transfer from TiO_2. The nanosecond spectra of the dyes adsorbed on the TiO_2 films resemble the spectral features of the femtosecond studies. Fig. 6 shows the nanosecond transient absorption spectra of **BF3a** and **F3b** for comparison. The singlet bleaching and the absorption maxima are comparable to those found throughout the femtosecond studies. The analysis of the decays

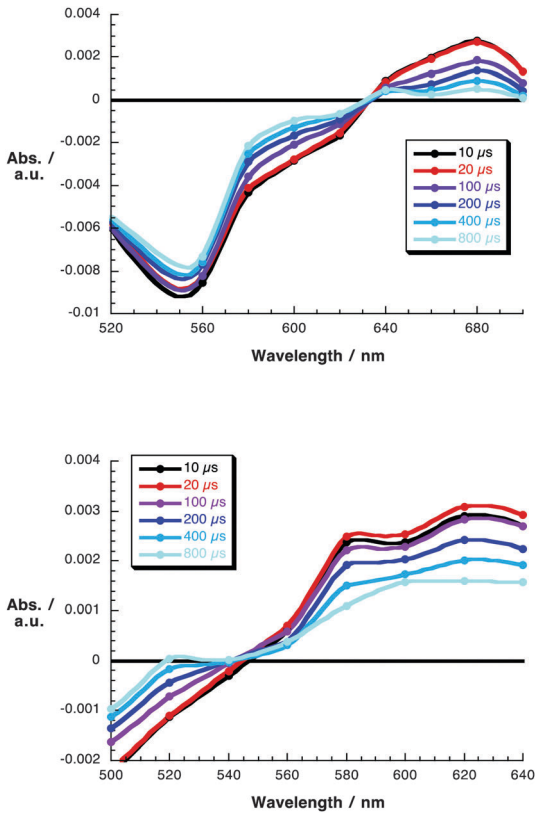

Fig. 6 Differential absorption spectra obtained upon nanosecond flash photolysis (λ_{exc} = 480 nm) of 3 μm-thick TiO_2 films sensitized with **BF3a** (top) and **F3b** (bottom) with several time delays at room temperature showing the spectral characteristics of the oxidized states and the slow charge recombination.

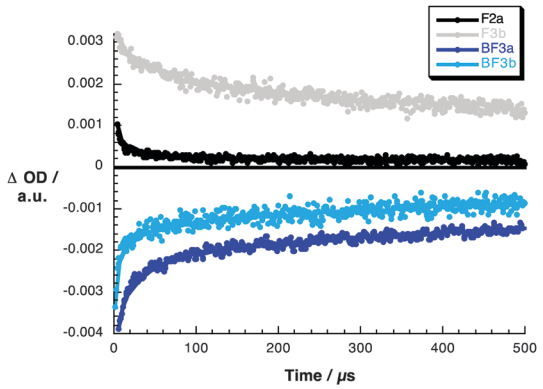

Fig. 7 Time absorption profiles at 600 nm of 3 μm-thick transparent TiO_2 films of **F2a**, **F3b**, **BF3a** and **BF3b** without electrolyte solution as obtained from nanosecond flash photolysis studies (λ_{exc} = 480 nm) at room temperature indicating the slow decay of the radical cation signal of **F3b**, **BF3a**, and **BF3b** as compared with **F2a**.

of the spectral signatures of the oxidized state allowed for the determination of the lifetimes of the oxidized states in the absence of the redox electrolyte. The lifetimes and the corresponding charge recombination rate constants are given in Table 3.

Without the redox electrolyte solution the decays of the signals at 600 nm follow an exponential behavior (Fig. 7) and give rise to lifetimes on the order of hundreds of microseconds for **F3b**, **BF3a** and **BF3b**. For **F2a**, the lifetime of the oxidized state decreases by two orders of magnitude to 6.5 μs. The reason for the very fast charge recombination in **F2a** is shown throughout the molecular modeling studies (*vide supra*). Altering the substitution pattern from *meta* to *para* directly affects the delocalization of the positive charge within the molecular framework (Fig. S44, ESI†). Therefore, in the oxidized state of **F2a** the positive charge is much more localized within the fluorene unit (+0.84*e*) as compared with **F3b** (+0.23*e*), **BF3a** (+0.19) and **BF3b** (+0.12*e*), which in turn results in a significant destabilization of the charge-separated species.

Importantly, upon addition of the redox electrolyte the oxidized states are regenerated on a much faster time-scale and the signals decay with accelerated dynamics – dye regeneration. As shown in Table 3, except for **F2a**, the charge recombination rates of the remaining dyes increase by two orders of magnitude. The reason for the increasing rates stems from the fact that in the presence of the electrolyte the oxidized species of the dyes are mainly reduced by electrons from the redox electrolyte solution, which occurs notably faster than the charge recombination from TiO_2. Due to very fast charge recombination in **F2a**, the dye regeneration rate constant is nearly invariant.

Photovoltaic studies: a proof of concept

Some preliminary photovoltaic experiments were conducted to evaluate the potential of employing these new molecules as sensitizers in DSSC devices. DSSC device fabrication details are

given in the Experimental section. The *J–V* curves of the devices are shown in Fig. S47 (ESI†). The photovoltaic parameters: the short-circuit current density (J_{sc}), the open-circuit photovoltage (V_{oc}), the fill factor (FF) and the overall power conversion efficiency (PCE) are tabulated in Table S3 (ESI†). The maximum PCE of 3.3% was obtained for the **BF3b**-sensitized device with a volatile-solvent-based electrolyte under AM 1.5G sunlight (100 mW cm^{-2}).

It is interesting to note the low efficiency values shown by **BF3a** and **BF3c** when compared with **BF3b** which exhibits the lower HOMO–LUMO gap. The relatively moderate values found for the PV parameters indicate that there are several factors that can be optimized in terms of electronic properties, light absorption and morphology to significantly improve the PV properties of these new molecules. In this regard, the introduction of additional methoxy or hexyloxy groups in the DPA units would extend the absorption region of organic dyes in the visible light while preventing charge recombination.[8] Nevertheless, these photovoltaic data reveal the interest of functionalized bi-fluorenylidenes for PV applications. However, a more precise design and the presence of efficient substituents are essential requirements in the search for efficient materials.

Conclusions

In summary, we have carried out the synthesis of a series of new fluorenes and bi-fluorenylidenes endowed with different electron donor and acceptor units in order to improve their electronic and optical properties as light-harvesters. The new fluorene derivatives have been synthesized in a multistep manner involving Buchwald and Knoevenagel reactions and the bi-fluorenylidenes through a Barton's coupling starting from fluorenones. All the new compounds have been fully characterized by spectroscopic techniques and by cyclic voltammetry. DFT theoretical calculations reveal relatively planar π-conjugated fluorene derivatives, whereas a dihedral angle of around 36° is found between the two fluorene units in bi-fluorenylidenes. For the fluorene dyes, calculations evidence a better electronic communication between the donor and acceptor moieties when the donor diphenylamine (DPA) substituents are linked to the fluorene core in *para* than in *meta* positions. The effect of the substitution pattern on the oxidation potentials and the relative stability of the resulting radical cations has been nicely rationalized on the basis of theoretical calculations. The attachment of DPA groups in *meta* positions increases the energy of the HOMO in a higher degree and leads to significantly more stable cations than *para* substitution. The π-extended bi-fluorenylidene core produces a relative stabilization of the radical cations compared with the analogous mono-fluorene dyes.

The electronic absorption spectra show the effect that the presence of electron-releasing and electron-withdrawing groups, as well as their *meta* or *para* position, has on the electronic structure of the fluorene and bi-fluorenylidene derivatives. Remarkably, the better optical performance of donor–acceptor bi-fluorenylidenes showing an intense broad band covering the 440–660 nm region is associated with CT excitations involving the donor units and the bi-fluorenylidene core. The inclusion of π-conjugated phenylenevinylene spacers to link the donor DPA groups is shown to improve the optical performance of the dyes.

Adsorption of chromophores on TiO_2 occurs with a blue-shift due to the deprotonation of the carboxylic anchoring groups, which confirms the connectivity of the organic addends to the TiO_2 surface.

The charge recombination process has been studied in the presence and in the absence of a redox electrolyte. Interestingly, the regeneration of the dyes' ground state occurs by back electron transfer from TiO_2 in the absence of electrolyte, whereas in the presence of electrolyte the oxidized species of the dyes are mainly reduced by the electrolyte in a significantly faster charge recombination process.

Finally, preliminary photovoltaic DSSCs measurements show that the new systems are photoactive showing values of power conversion efficiencies as high as 3.3% obtained for the most π-extended **BF3b** bi-fluorenylidene compound under AM 1.5 G sunlight conditions.

Acknowledgements

M. W. and J.-E. M. thank NCCR MUST, a research instrument of the Swiss National Science Foundation for generous support. This work has been supported by the MINECO of Spain (CTQ 2011-27934, CTQ2012-30668, CTQ2012-31914, CTQ2014-52045-R, CTQ2015-71936-REDT, and MDM2015-0538), Comunidad de Madrid (FOTOCARBON project S2013/MIT-2841), Generalitat Valenciana (PROMETEO/2012/053), European Feder funds (CTQ2012-31914) and ERC-320441-Chiralcarbon. N. M. thanks the Alexander von Humboldt Foundation. J. C. akcnowledges the MECD of Spain for an FPU predoctoral grant. JLD akcnowledges Ikerbasque, the Basque Foundation for Science, for a "Ikerbasque Research Fellow" contract, the Polymat Foundation and the Basque Government (PC2015-1-03 (16-79)).

Notes and references

1 (*a*) Z. Yu and L. Sun, *Adv. Energy Mater.*, 2015, **5**, 1500213; (*b*) S. F. Völker, S. Collavini and J. L. Delgado, *ChemSusChem*, 2015, **8**, 3012; (*c*) S. Collavini, S. F. Völker and J. L. Delgado, *Angew. Chem., Int. Ed.*, 2015, **54**, 9757; (*d*) L. Cabau, I. Garcia-Benito, A. Molina-Ontoria, N. F. Montcada, N. Martin, A. Vidal-Ferran and E. Palomares, *Chem. Commun.*, 2015, **51**, 13980.

2 (*a*) M. Grätzel, *Nature*, 2001, **414**, 338; (*b*) B. O'Regan and M. Grätzel, *Nature*, 1991, **353**, 737.

3 (*a*) A. Hagfeldt and M. Grätzel, *Chem. Rev.*, 1995, **95**, 49; (*b*) M. Grätzel, U. Bach, D. Lupo, P. Comte, J. E. Moser, F. Weissrtel, J. Salbeck and H. Spreitzer, *Nature*, 1998, **395**, 583; (*c*) M. K. Nazeeruddin, S. M. Zakeeruddin, J.-J. Lagref, P. Liska, P. Comte, C. Barolo, G. Viscardi, K. Schenk and M. Grätzel, *Coord. Chem. Rev.*, 2004, **248**, 1317.

4 J. Burschka, N. Pellet, S.-J. Moon, R. H. Baker, P. Gao, M. K. Nazeeruddin and M. Grätzel, *Nature*, 2013, **499**, 316.
5 (*a*) Z. Chen, F. Li and C. Huang, *Curr. Org. Chem.*, 2007, **11**, 1241; (*b*) P. Xie and F. Guo, *Curr. Org. Chem.*, 2007, **11**, 1272; (*c*) N. Robertson, *Angew. Chem., Int. Ed.*, 2006, **118**, 2398.
6 (*a*) Y. Ooyama and Y. Harima, *Eur. J. Org. Chem.*, 2009, 2903; (*b*) Z. Ning and H. Tian, *Chem. Commun.*, 2009, 5483; (*c*) A. Mishra, M. K. R. Fischer and P. Bäuerle, *Angew. Chem.*, 2009, **121**, 2510; (*d*) A. Mishra, M. K. R. Fischer and P. Bäuerle, *Angew. Chem., Int. Ed.*, 2009, **48**, 2474; (*e*) Z. Ning, Y. Fu and H. Tian, *Energy Environ. Sci.*, 2010, **3**, 1170; (*f*) J.-H. Yum, E. Baranoff, S. Wenger, M. K. Nazeeruddin and M. Grätzel, *Energy Environ. Sci.*, 2011, **4**, 842; (*g*) F. Odobel, L. L. Pleux, Y. Pellegrin and E. Blart, *Acc. Chem. Res.*, 2010, **43**, 1063; (*h*) H. Imahori, T. Umeyama and S. Ito, *Acc. Chem. Res.*, 2009, **42**, 1809; (*i*) X.-F. Wang and H. Tamiaki, *Energy Environ. Sci.*, 2010, **3**, 94; (*j*) W. Zhang, Z. Feng, M. Su, M. Saeys and B. Liu, *Macromol. Rapid Commun.*, 2009, **30**, 1533; (*k*) Z. Fang, A. A. Eshbaugh and K. S. Schanze, *J. Am. Chem. Soc.*, 2011, **133**, 3063; (*l*) D. W. Chang, S.-J. Ko, J. Y. Kim, S.-M. Park, H. J. Lee, L. Dai and J.-B. Baek, *Macromol. Rapid Commun.*, 2011, **32**, 1809.
7 (*a*) S. Wenger, P.-A. Bouit, Q. Chen, J. Teuscher, D. Di Censo, R. Humphry-Baker, J. E. Moser, J. L. Delgado, N. Martín, S. M. Zakeeruddin and M. Grätzel, *J. Am. Chem. Soc.*, 2010, **132**, 5164; (*b*) P.-A. Bouit, M. Marszalek, R. Humphry-Baker, R. Viruela, E. Ortí, S. M. Zakeeruddin, M. Grätzel, J. L. Delgado and N. Martín, *Chem. – Eur. J.*, 2012, **18**, 11621; (*c*) C. A. Echeverry, M. A. Herranz, A. Ortiz, B. Insuasty and N. Martín, *New J. Chem.*, 2014, **38**, 5801; (*d*) P.-A. Bouit, C. Villegas, J. L. Delgado, P. Viruela, R. Pou-Amérigo, E. Ortí and N. Martín, *Org. Lett.*, 2011, **13**, 604; (*e*) P.-A. Bouit, L. Infantes, J. Calbo, R. Viruela, E. Ortí, J. L. Delgado and N. Martín, *Org. Lett.*, 2013, **15**, 4166.
8 A. Hagfeldt, G. Boschloo, L. Sun, L. Kloo and H. Pettersson, *Chem. Rev.*, 2010, **110**, 6595.
9 (*a*) C.-H. Chen, Y.-C. Hsu, H.-H. Chou, K. R. J. Thomas, J. T. Lin and C.-P. Hsu, *Chem. – Eur. J.*, 2010, **16**, 3184; (*b*) W. Li, Y. Wu, X. Li, Y. Xie and W. Zhu, *Energy Environ. Sci.*, 2011, **4**, 1830; (*c*) A. Baheti, P. Tyagi, K. R. J. Thomas, Y.-C. Hsu and J. T. Lin, *J. Phys. Chem. C*, 2009, **113**, 8541; (*d*) C.-G. Wu, M.-F. Chung, H.-H. G. Tsai, C.-J. Tan, S.-C. Chen, C.-H. Chang and T.-W. Shih, *ChemPlusChem*, 2012, **77**, 832.
10 F. G. Brunetti, X. Gong, M. Tong, A. J. Heeger and F. Wudl, *Angew. Chem., Int. Ed.*, 2010, **49**, 5332.
11 C.-Y. Chiu, H. Wang, F. G. Brunetti, F. Wudl and C. J. Hawker, *Angew. Chem., Int. Ed.*, 2014, **53**, 3996.
12 P. J. Stephens, F. J. Devlin, C. F. Chablowski and M. J. Frisch, *J. Phys. Chem. A*, 1994, **98**, 11623.
13 J. T. H. Dunning, *J. Chem. Phys.*, 1989, **90**, 1007.
14 M. J. Frisch, G. W. Trucks, H. B. Schlegel, G. E. Scuseria, M. A. Robb, J. R. Cheeseman, G. Scalmani, V. Barone, B. Mennucci, G. A. Petersson, H. Nakatsuji, M. Caricato, X. Li, H. P. Hratchian, A. F. Izmaylov, J. Bloino, G. Zheng, J. L. Sonnenberg, M. Hada, M. Ehara, K. Toyota, R. Fukuda, J. Hasegawa, M. Ishida, T. Nakajima, Y. Honda, O. Kitao, H. Nakai, T. Vreven, J. A. Montgomery Jr, J. E. Peralta, F. Ogliaro, M. Bearpark, J. J. Heyd, E. Brothers, K. N. Kudin, V. N. Staroverov, R. Kobayashi, J. Normand, K. Raghavachari, A. Rendell, J. C. Burant, S. S. Iyengar, J. Tomasi, M. Cossi, N. Rega, N. J. Millam, M. Klene, J. E. Knox, J. B. Cross, V. Bakken, C. Adamo, J. Jaramillo, R. Gomperts, R. E. Stratmann, O. Yazyev, A. J. Austin, R. Cammi, C. Pomelli, J. W. Ochterski, R. L. Martin, K. Morokuma, V. G. Zakrzewski, G. A. Voth, P. Salvador, J. J. Dannenberg, S. Dapprich, A. D. Daniels, O. Farkas, J. B. Foresman, J. V. Ortiz, J. Cioslowski and D. J. Fox, *Gaussian 09, Revision C.01*, Gaussian Inc., Wallingford, CT, 2009.
15 (*a*) M. E. Casida, C. Jamorski, K. C. Casida and D. R. Salahub, *J. Chem. Phys.*, 1998, **108**, 4439; (*b*) C. Jamorski, M. E. Casida and D. R. Salahub, *J. Chem. Phys.*, 1996, **104**, 5134; (*c*) M. Petersilka, U. J. Gossmann and E. K. U. Gross, *Phys. Rev. Lett.*, 1996, **76**, 1212.
16 (*a*) J. Tomasi and M. Persico, *Chem. Rev.*, 1994, **94**, 2027; (*b*) J. Tomasi, B. Mennucci and R. Cammi, *Chem. Rev.*, 2005, **105**, 2999.
17 http://www.chemcraftprog.com.
18 H. Le Moal, R. Carrie, A. Foucaud, R. Danion-Bougot and C. Gadreau, *Bull. Soc. Chim. Fr.*, 1968, **5**, 2156.
19 S. Scheibye, R. Shabana, S.-O. Lawesson and C. Roemming, *Tetrahedron*, 1982, **38**, 993.

Electronic Supplementary Material (ESI) for Journal of Materials Chemistry C.

Supporting Information

Efficient Light-Harvesters Based on Modified Bi-fluorenylidenes.

Mateusz Wielopolski,[a] Magdalena Marszalek, [b] Fulvio G. Brunetti, [c] Damien Joly, [c] Joaquín Calbo,[d] Juan Aragó, [d] Jacques-E. Moser,[a] Robin Humphry-Baker,[b] Shaik M. Zakeeruddin,[b] Juan Luis Delgado,*[e,f] Michael Grätzel,*[b] Enrique Ortí,*[d] and Nazario Martín,*[c,g]

[a] Photochemical Dynamics Group, Institute of Chemical Sciences and Engineering, Ecole Polytechnique Fédérale de Lausanne, CH-1015 Lausanne, Switzerland.

[b]Laboratory for Photonics and Interfaces, Institute of Chemical Sciences and Engineering, Swiss Federal Institute of Technology, CH-1015 Lausanne, Switzerland. E-mail: *michael.graetzel@epfl.ch*

[c] IMDEA-Nanoscience, Ciudad Universitaria de Cantoblanco, 28049 Madrid, Spain.

[d] Instituto de Ciencia Molecular, Universidad de Valencia, 46980 Paterna, Spain. E-mail: *enrique.orti@uv.es*

[e] POLYMAT, University of the Basque Country UPV/EHU, Avenida de Tolosa 72, 20018 Donostia-San Sebastian, Spain. E-mail: *juanluis.delgado@polymat.eu*

[f] Ikerbasque, Basque Foundation for Science, 48011 Bilbao, Spain.

[g] Departamento de Química Orgánica, Facultad de Ciencias Químicas, Universidad Complutense de Madrid, 28040 Madrid, Spain. E-mail: *nazmar@quim.ucm.es*

1. General

NMR spectra (^{1}H, ^{13}C) were recorded at room temperature on Bruker DPX 300 MHz and Bruker AVIII. 500 MHz data are listed in parts per million (ppm) and are reported relative to tetramethylsilane (^{1}H, ^{13}C). Mass spectrometry was carried out by the services at the Universidad Complutense de Madrid. UV-vis spectra were recorded in a Varian Cary 50 spectrometer at a constant temperature of 25 °C in diluted dimethylsulfoxide solution (ca. 10^{-5} mol L^{-1}). Compounds **F1**,[1] **1**,[2] **2**,[3] **3**,[4] **10**,[5] and **13**[6] were synthesized according to already described procedures.

2-Synthesis of fluorene derivatives (F series)

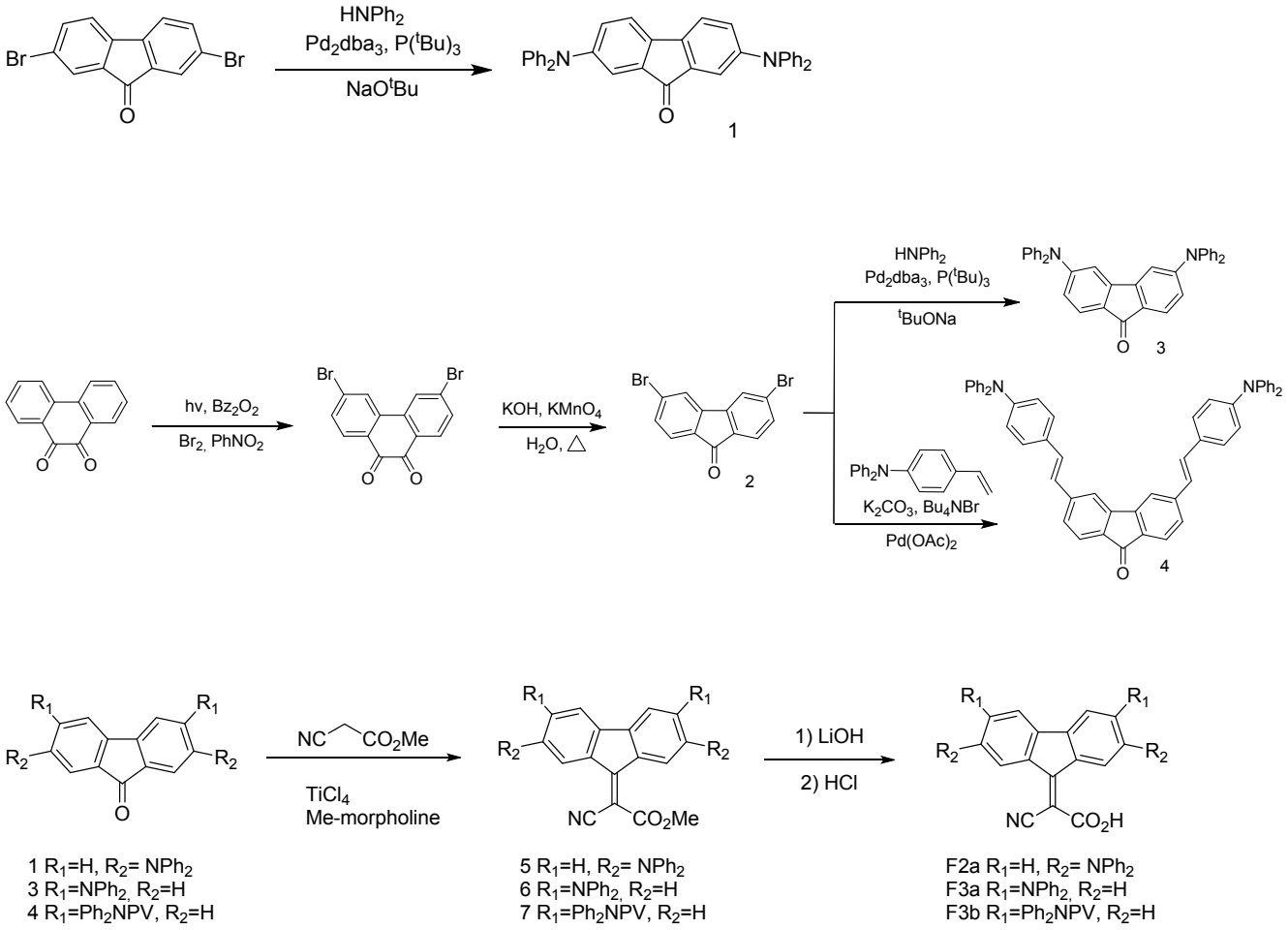

Scheme S1. Synthesis of **F2a**, **F3a**, and **F3b**.

2.1 Synthesis of fluorenone derivatives

4: **2** (60 mg, 0.17 mmol), *n*-Bu_4NBr (112 g, 0.35 mmol), K_2CO_3 (100 g, 0.71 mmol) and diphenyl-(4-vinyl-phenyl)-amine (54 g, 0.2 mmol) were dissolved in 25 mL of dry DMF under argon atmosphere. $Pd(OAc)_2$ (catalytic amount, 2–3 % mmol) was then added under an argon flow. The mixture was heated at 80–90 °C overnight. The crude was poured in water to precipitate **4** that was then filtered. Purification by column chromatography over silica gel afford **4** as a red solid (53 % yield).

^{1}H-NMR (300 MHz, $CDCl_3$): δ ppm 7.63 (s, 2H), 7.55 (d, 2H, J = 7.7 Hz), 7.35 (d, 4H, J = 8.5 Hz), 7.29 (s, 1H), 7.23-7.18 (m, 10H), 7.13 (s, 1H), 7.07-6.92 (s, 18H). ^{13}C-NMR (75 MHz, $CDCl_3$): δ ppm 148.3, 147.5, 144.7, 144.2, 133.9, 131.3, 130.6, 129.5, 127.9, 127.5, 126.1, 125.0, 124.8, 123.6, 123.1, 117.5. MS: (ESI^+); calculated*: m/z* 718.30; found *m/z*: 741.3 $[M+Na]^+$, 742.3 $[M+H+Na]^+$. IR: 1736, 1700, 1587, 1496, 1324, 1281, 754, 668.

2.2 General procedure for Knoevenagel condensation:

Compounds **5**, **6**, and **7** were successfully obtained only in neat conditions. The use of solvents, such as DCM or chloroform yielded only traces of the titled compounds. The corresponding ketones were dissolved in 10 eq of cyano-acetic acid methyl ester, 4-methyl-morpholine (10 eq). Then $TiCl_4$ (10 eq) was carefully added dropwise, *via* a syringe. The reaction was performed in vial or in a 10mL schlenk flask. After the addition of $TiCl_4$, the reaction was gently heated at 60 °C until no more starting materials was observed by TLC. The crude was poured in water (100 mL) and extracted with DCM (2 × 25 mL). In case of emulsion, the solution was filter over celite and ammonium chloride was added to the water phase. The organic layers were collected, dried over $MgSO_4$ and the solvent removed under reduced pressure. The crude solid was purified by chromatography column (hexanes / DCM; 3 : 7 in all cases). The target compound, which contained a large excess of cyano-acetic acid methyl ester, was further purified by washing with MeOH, giving pure derivatives **5**, **6**, and **7**. Relative low yields are reported as follows due to the additional purification process.

5: a bluish green solid was obtained (47 % yield)

^{1}H-NMR (500 MHz, $CDCl_3$): δ ppm 8.19 (bs, 2H), 7.4–7.1 (m, 24H), (3.5, s, 3H); ^{13}C-NMR (125 MHz, $CDCl_3$): δ ppm 152.9, 147.45, 136.5, 135.6, 129.5, 127.3, 124.5, 122.1, 121.6, 123.4, 120.0, 115.4, 53.2MS: (ESI^-); calculated*: m/z* 595.23; found: *m/z*: 537.0 [M-$COOCH_3$], 568.1 [M-CN]. IR: 3031, 2925, 2856, 2205, 1588, 1489, 1462, 1322, 1274, 754, 696.

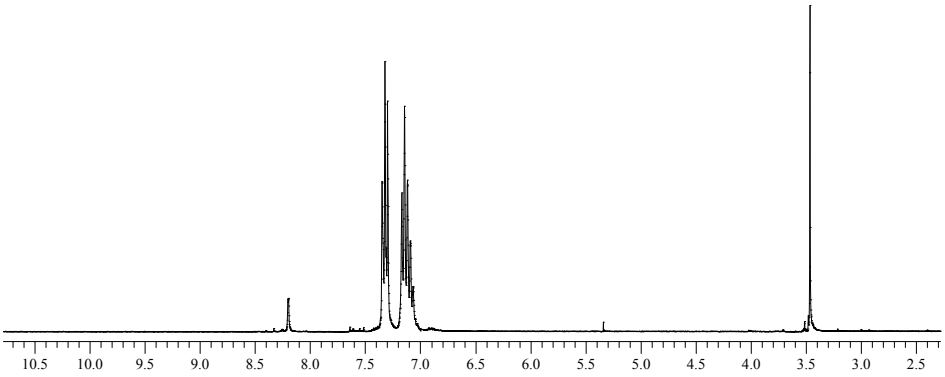

Figure S1. ^{1}H-NMR of compound **5.**

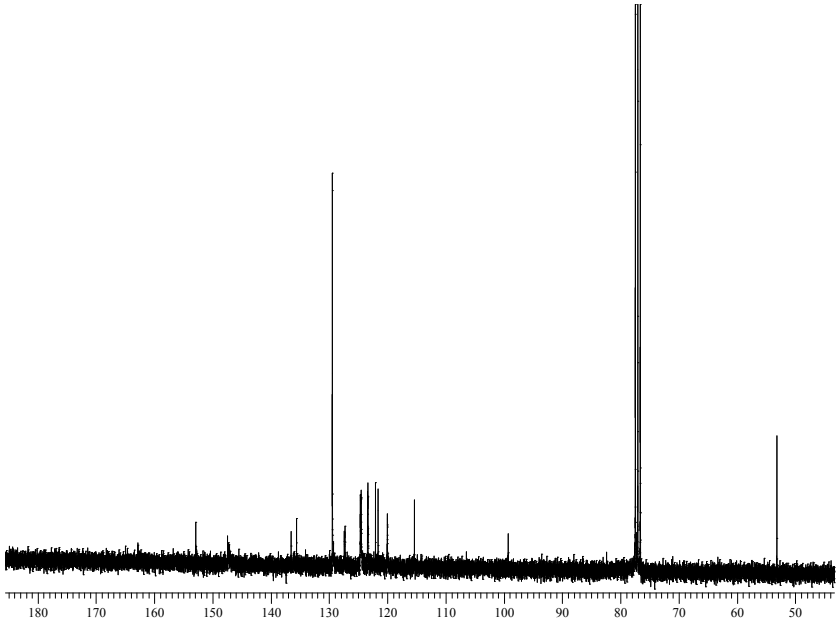

Figure S2. ^{13}C-NMR of compound **5.**

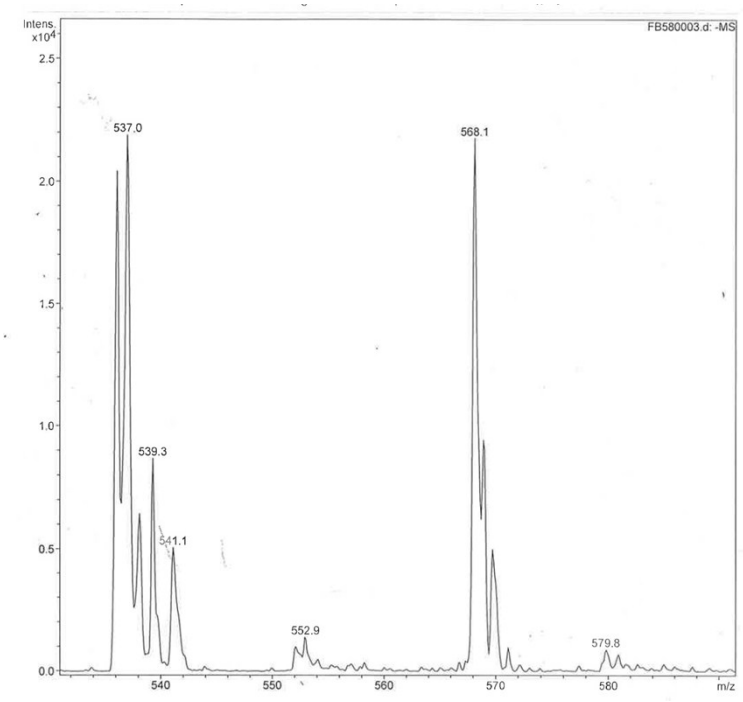

Figure S3. MS of compound **5.**

6: a dark solid was obtained (43 % yield).

^{1}H-NMR (500 MHz, $CDCl_3$): δ ppm 8.40 (d, 1H, J_3 = 8.5 Hz), 8.14 (d, 1H, J_3 = 8.7 Hz), 7.30–7.27 (m, 8H), 7.12–7.09 (m, 12H), 6.98 (dd, 2H, J_3 = 10.8 Hz, J_4 = 2.0 Hz), 6.77 (dd, 1H, J_3 = 8.8 Hz, J_4 = 2.2 Hz), 6.69 (dd, 1H, J_3 = 8.7 Hz, J_4 = 2.2 Hz), 3.91 (s, 3H); ^{13}C-NMR (125 MHz, $CDCl_3$): δ ppm 164.2, 156.4, 152.2, 152.1, 146.6, 146.5, 143.9, 143.6, 130.7, 129.7, 128.5, 128.1, 125.9, 125.8, 125.7, 124.7, 120.9, 120.5, 118.5, 112.7, 112.4, 92.8, 53.1; MS: (ESI$^+$); calculated*:* *m/z* 595.23; found: *m/z*: 618.3 $[M+Na]^+$, 634.3 $[M+K]^+$. IR: 3062, 2924, 2855, 2204, 1726, 1586, 1489, 1276, 1238, 1099, 760, 698.

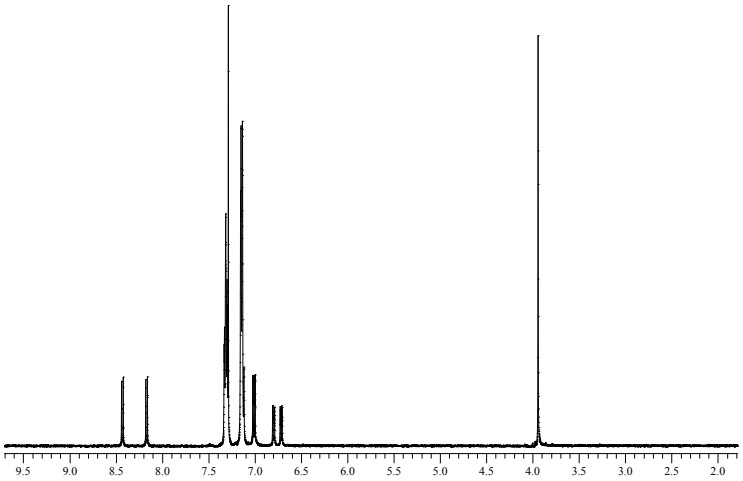

Figure S4. ^{1}H-NMR of compound **6.**

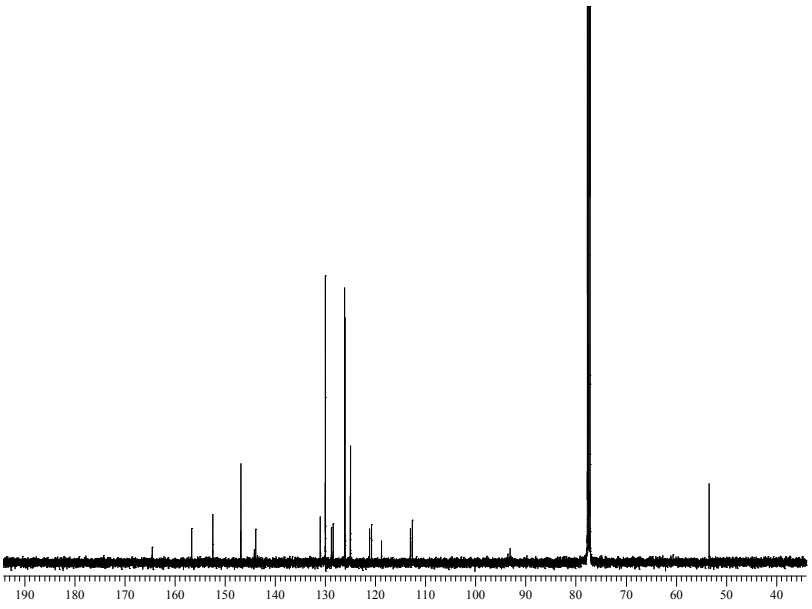

Figure S5. ^{13}C-NMR of compound **6.**

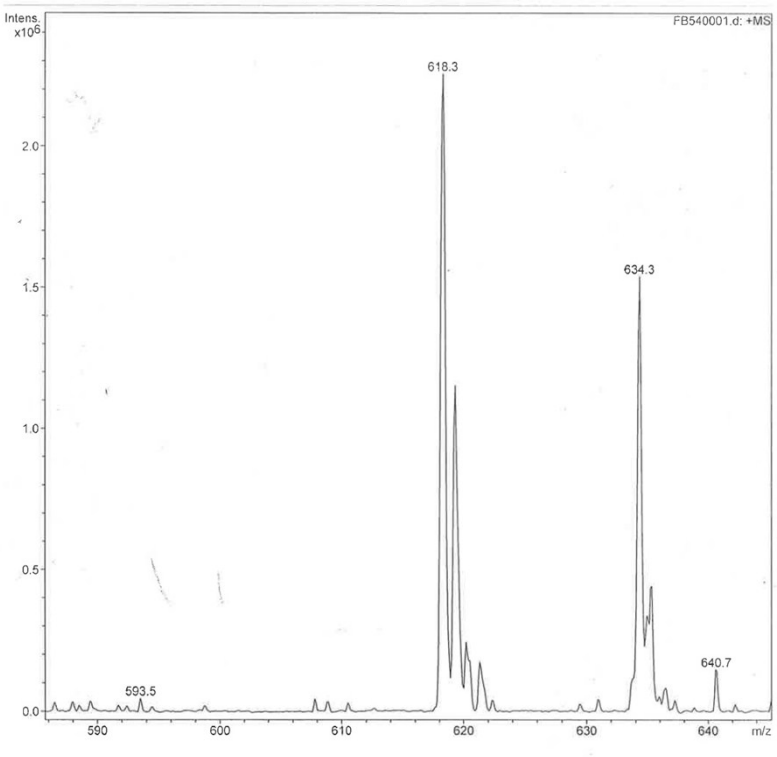

Figure S6. MS of compound **6.**

7: a dark solid was obtained (37 % yield).

^{1}H-NMR (500 MHz, $CDCl_3$): δ ppm 8.54 (d, 1H, J_3 = 13 Hz), 8.16 (d, 1H, J_3 = 13 Hz), 7.73 (d, 2H, J_3 = 8 Hz), 7.45–7.41 (m, 4H), 7.38–7.35 (m, 2H), 7.31–7.28 (m, 7H), 7.22 (d, 1H, J_3 = 5.6 Hz), 7.14–7.05 (m, 18H), 6.99 (d, 2H, J_3 = 10.5 Hz), 4.00 (s, 3H). ^{13}C-NMR (125 MHz, $CDCl_3$): δ ppm 163.8, 156.2, 148.6, 147.7, 143.2, 142.9, 135.4, 134.3, 131.5, 131.4, 130.8, 130.9, 129.8, 128.3, 127.5, 127.3, 127.0, 126.2, 125.3, 123.9, 123.8, 123.4, 123.3, 117.7, 117.4, 117.3, 97.3; MS: (ESI^+); calculated*: m/z* 799.32; found: *m/z*: 822.3$[M+Na]^+$; 823.4 $[M+H+Na]^+$, IR: 3030, 1730, 1541, 1497, 1280, 1236, 1180, 1100, 959, 831, 754, 665.

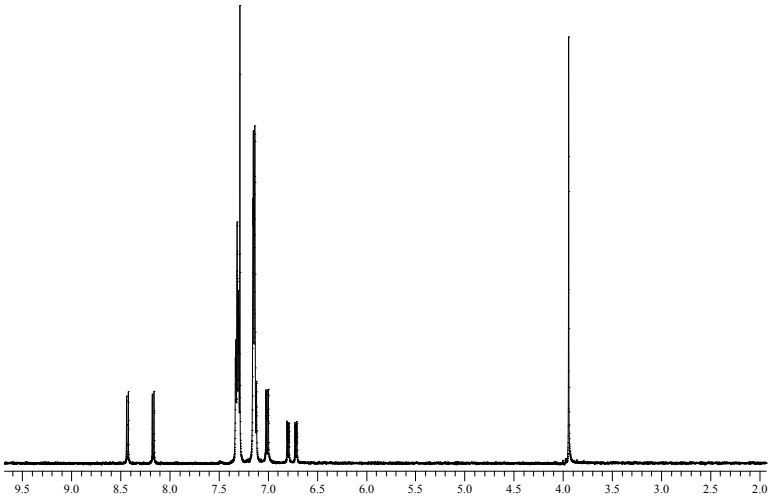

Figure S7. ^{1}H-NMR of compound **7.**

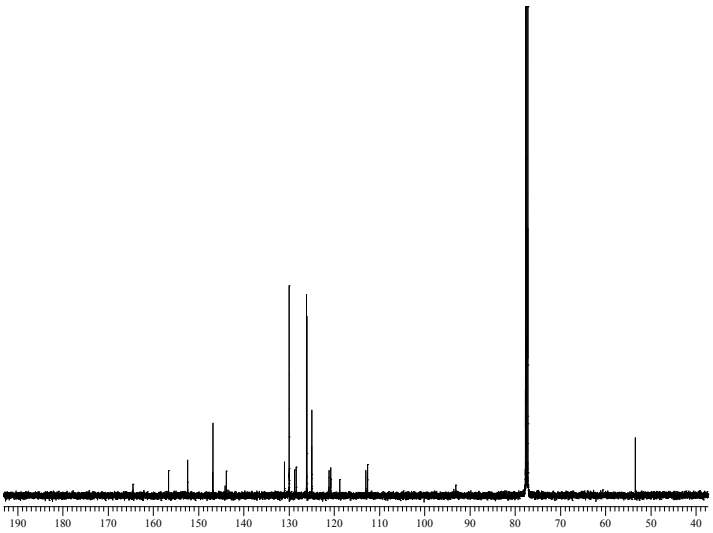

Figure S8. ^{13}C-NMR of compound **7.**

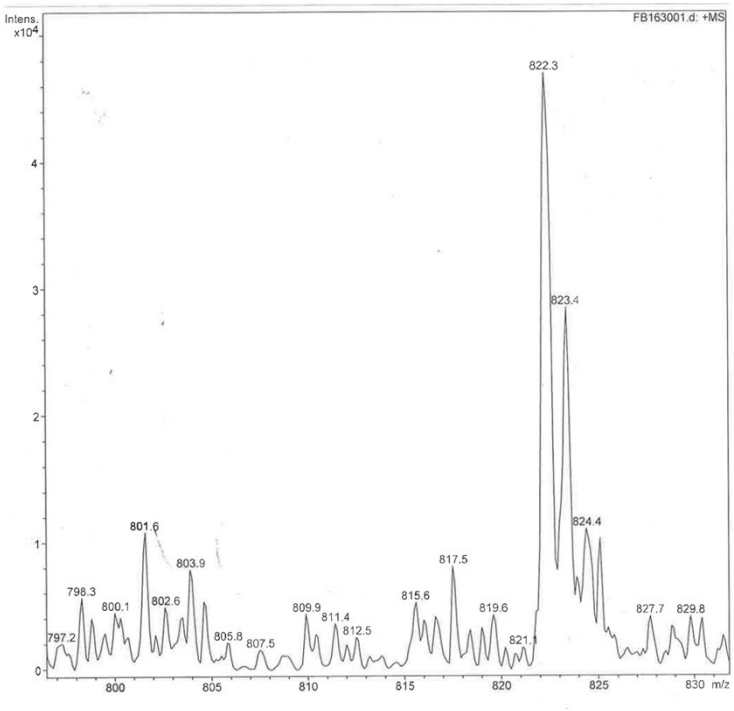

Figure S9. MS of compound **7.**

2.3 Hydrolysis of esters

*Due to intrinsic solubility issues of some of the described final materials (**F2a**, **F3a** and **F3b**), its complete characterization by NMR techniques was difficult to perform. However in all these materials, it is possible to appreciate the disappearance of the methoxy group, therefore confirming the hydrolysis of the esters. Additionally, it is important to remark here, that those materials difficult to study by NMR were correctly characterized by MS, HR-MS and FT-IR techniques.*

F2a: ester derivative **5** (0.18 mmol) was dissolved in CH_3CN (30 mL) and treated with LiOH (excess, 86.4 mg, 3.6 mmol) dissolved in water (10 mL). The reaction was stirred at RT for 5–6 hrs and monitored by TLC (eluent mixture: DCM : hexanes; 1 : 1). Acetonitrile was removed under reduced pressure and the crude was extracted with AcOEt (3 × 25 mL) and a 10 % HCl water solution. The combined organic layers were dried over $MgSO_4$ and concentrated affording bluish green solid **F2a** (% yield).

^{1}H-NMR (500 MHz, $CDCl_3$): δ ppm 8.2 (bs, 2H), 7.7 (bs, 2H), 7.4–6.9 (m, 22H); MS: (ESI^-); calculated*: m/z* 581.21; found: *m/z*: 604.2 $[M+Na]^-$, 620.1 m/z: $[M+K]^-$; HR MS: (ESI^-); calculated*: m/z* 581.2103; found: *m/z*: 581.2079 $[M]^+$; IR: 3031, 2925, 2856, 2205, 1588, 1489, 1462, 1322, 1274, 754, 696.

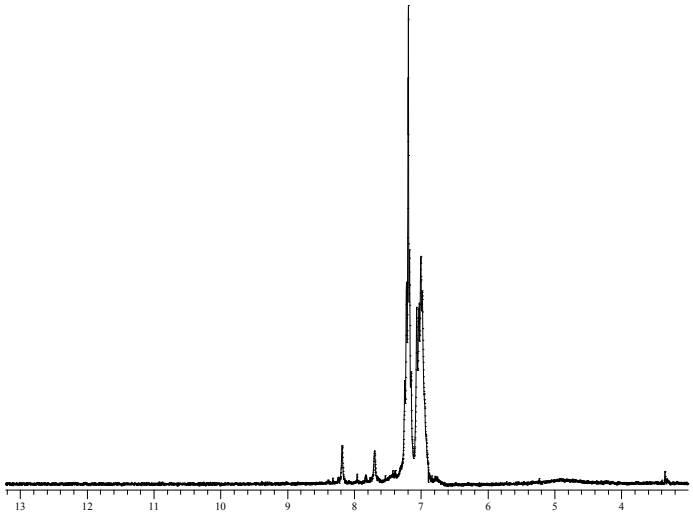

Figure S10. ^{1}H-NMR of compound **F2a.**

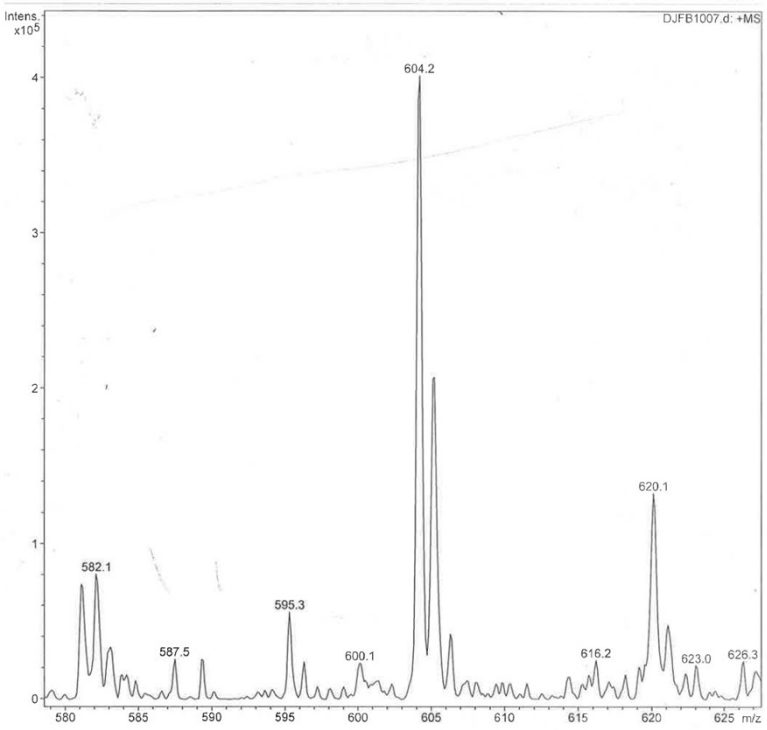

Figure S11. MS of compound **F2a.**

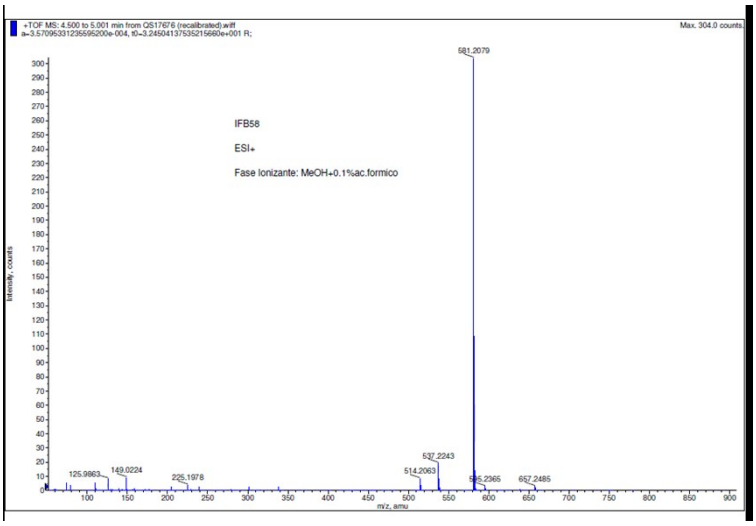

Figure S12. HR MS of compound **F2a.**

F3a: ester derivative **6** (0.20 mmol) was dissolved in 40 mL of a CH_3CN / methanol (1:1 v/v) solvent mixture and treated with an excess of NaOH (20–25 mL of a 3M water solution). The reaction was gently heated at 40–50 °C until no more ester was observed by TLC. Acetonitrile and methanol were removed under reduced pressure and the crude was extracted with DCM (3 × 30 ml) and a 10 % HCl solution. The organic layers were gathered, dried over Na_2SO_4, and evaporated under reduced pressure. The solid was washed with cyclohexane affording dark solid **F3a** (yield 42 %).

^{1}H-NMR (500 MHz, $CDCl_3$): δ ppm 8.40 (d, 1H, J_3 = 8.5 Hz), 8.20 (d, 1H, J_3 = 8.7 Hz), 7.30–7.27 (m, 8H), 7.12–7.09 (m, 12H), 6.98 (m, 2H), 6.77 (dd, 1H, J_3 = 8.8 Hz, J_4 = 2.2 Hz), 6.69 (dd, 1H, J_3 = 8.7 Hz, J_4 = 2.2 Hz); MS: (ESI^-); calculated*:* *m/z* 581.66; found: *m/z*:535.9 $[M\text{-}COOH]^+$; IR: broad 3367, 3051, 2923, 2855, 2198, 1692, 1587, 1489, 1276, 754, 696.

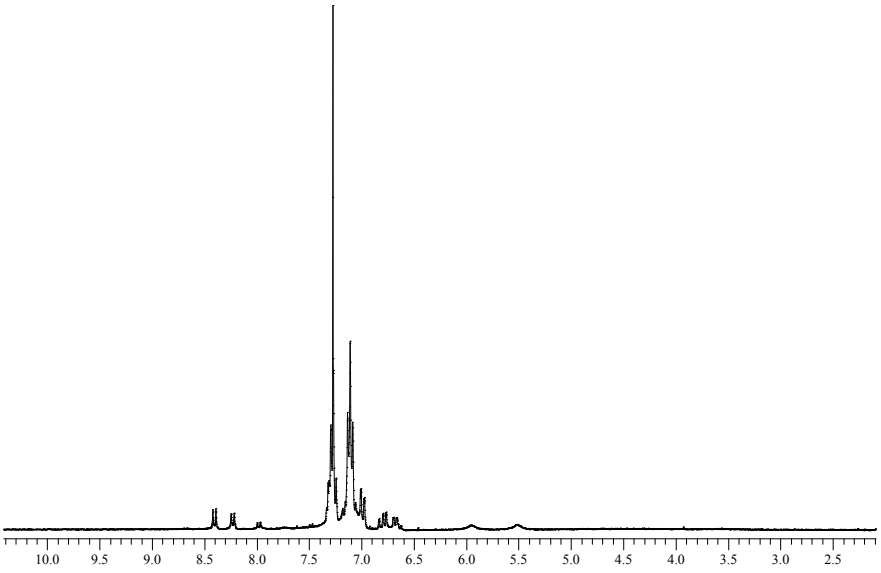

Figure S13. ^{1}H-NMR of compound **F3a.**

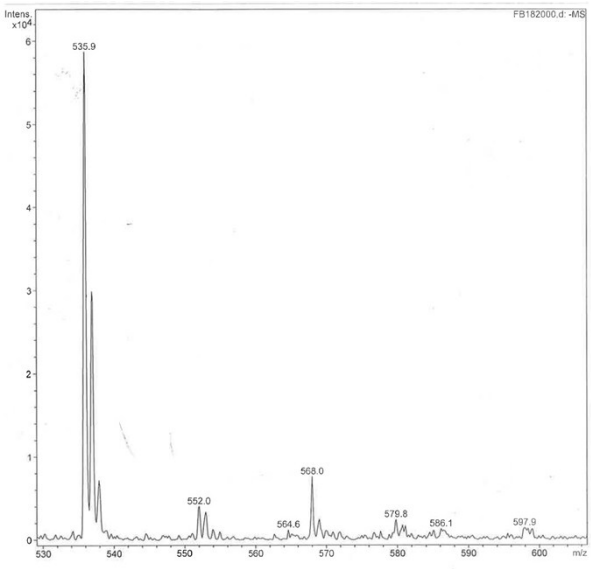

Figure S14. MS of compound **F3a.**

F3b: ester derivative **7** (0.20 mmol) was dissolved in 40 mL of a CH_3CN / methanol (1:1 v/v) solvent mixture and treated with an excess of NaOH (20–25 mL of a 3M water solution). The reaction was gently heated at 40–50 °C until no more ester was observed by TLC. Acetonitrile and methanol were removed under reduced pressure and the crude was extracted with DCM (3 × 30 ml) and a 10 % HCl solution. The organic layers were gathered, dried over Na_2SO_4, and evaporated under reduced pressure. The solid was washed with cyclohexane and pentane, **F3b** (yield 8 8%).

^{1}H-NMR (500 MHz, $CDCl_3$): δ ppm 8.05 (bs, 2H), 7.73 (bs, 2H), 7.5-6.9 (m, 34H); MS: (ESI^-); calculated*: m/z* 785.93; found: *m/z*: 740.1 $[M\text{-}COOH]^+$; IR: broad 3359, 3199, 2201, 1663, 1619, 1394, 753, 696.

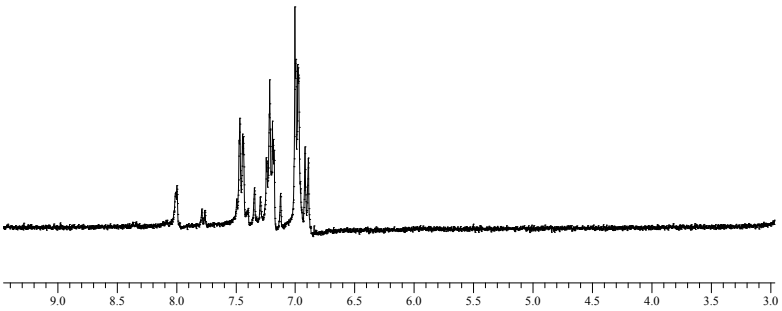

Figure S15. ^{1}H-NMR of compound **F3b.**

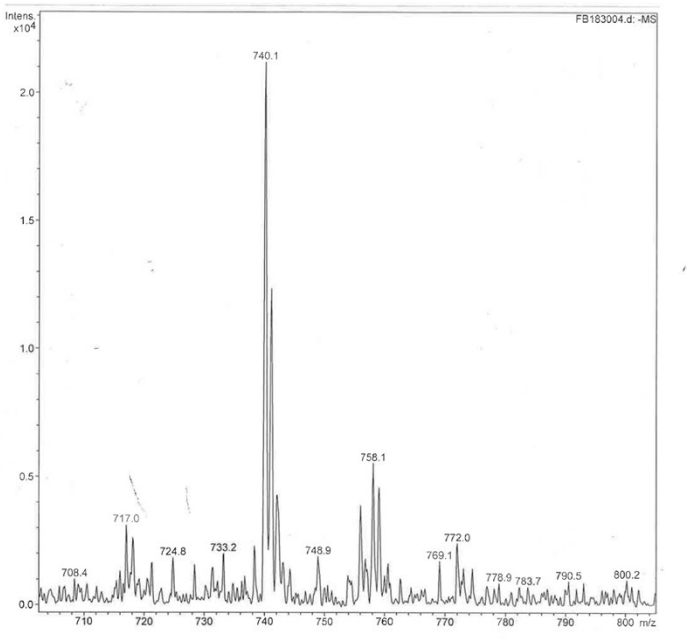

Figure S16. MS of compound **F3b.**

3 Synthesis of 9'9-fluorenylidene derivatives (BF series)

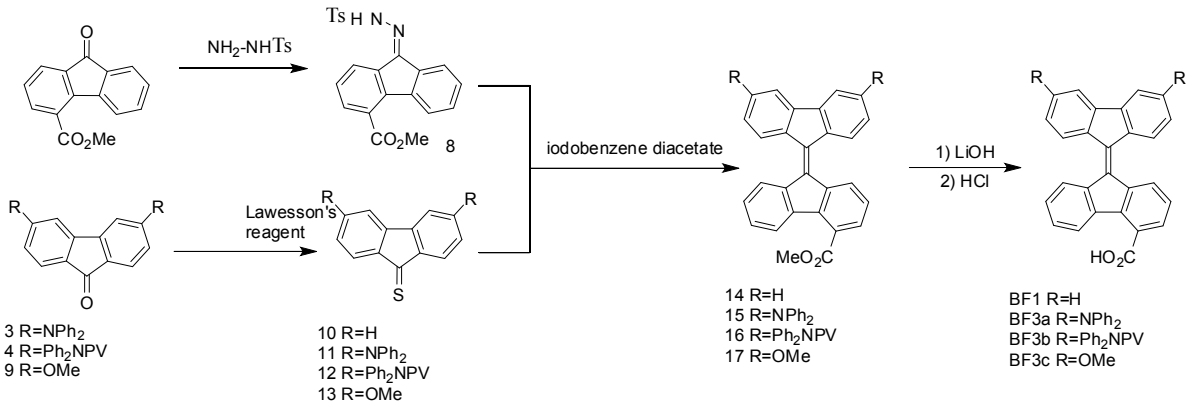

Scheme S2. Synthesis of **BF1**, **BF3a**, **BF3b**, and **BF3c**.

3.1 Synthesis of tosylhydrazone

8: 4-carboxymethyl fluoren-9-one (1.0 g, 4.2 mmol), was refluxed in methanol in the presence of tosylhydrazine (1.2 g; 6.3 mmol) and a catalytic amount of HCl (36%). After heating for a few hours the suspension turned pale yellow. TLC (eluent : DCM) was used to monitor the reaction. The cooled solution gave a pale yellow precipitate of **8** that was filtered on Buchner. (1.4 g, yield 82%).

^{1}H-NMR (500 MHz, [D$_6$]DMSO): δ ppm mixture of isomers: 8,33 (dd, J_3 = 8 Hz, J_4 = 1 Hz), 8,18 (dd, J_3 = 7 Hz, J_4 = 1.0 Hz), 8.15 (dd, J_3 = 9 Hz, J_4 = 1.0 Hz), 7,95–7.93 (m), 7,82 (dd, J_3 = 7 Hz, J_4 = 1.0 Hz), 7.77 (dd, J_3 = 8 Hz, J_4= 1 Hz), 7.64 (dd, J_3= 7 Hz, J_4 = 0.4 Hz), 7.58–7.50 (m), 7.47–7.42 (m), 7.38 (td, J_3 = 7 Hz, J_4 = 1 Hz), 3.96 (s), 3.94 (s), 2.39 (s). ^{13}C-NMR (125 MHz, [D$_6$]DMSO): δ ppm mixture of isomers: 167.5, 167.4, 150.0, 150.0, 143.9, 143.9, 139.6, 139.4, 137.5, 137.5, 137.4, 136.6, 135.0, 135.0, 132.2, 131.8, 131.7, 130.8, 130.5, 130.2, 129.5, 129.4, 129.1, 128.9, 128.3, 128.1, 128.0, 128.0, 127.6, 126.7, 126.4, 124.6, 124.5, 124.2, 121.2, 52.6, 20.99. MS: (ESI$^-$); calculated*: m/z* 406.10; found: *m/z*: 404.8 [M-H]$^-$. IR: 2923, 2855, 1708, 1596, 1439, 1343, 1276, 1168, 957, 879, 816, 772, 735, 682.

3.2 Synthesis of fluroene-thione derivatives

11: the corresponding fluorenone derivative **3** (103 mg, 0.2 mmol) and Lawesson's reagent (80 mg, 0.2 mmol) were heated in toluene (100 mL) at 90–100 °C for 5–6 hrs. The reaction was protected from the light with aluminum foil and monitored by TLC (hexanes/DCM 1:1). The solvent was removed under reduced pressure and the residue purified by chromatography column over silica gel (eluent: hexanes/DCM 1 : 1) to afford brown solid **11** (67% yield).

^{1}H-NMR (500 MHz, $CDCl_3$): δ ppm 7.63 (d, 2H, J_3 = 8.3 Hz), (s, 2H), 7.32–7.29 (m, 8H), 7.15–7.11 (m, 12H), 6.94 (d, 2H, J_1 = 1.9 Hz), 6.73 (d, 2H, J_3 = 8.3 Hz, J_4 = 1.9 Hz). ^{13}C-NMR (125 MHz, $CDCl_3$): δ ppm 219.68, 153.3, 146.7, 144.7, 136.6, 129.7, 125.8, 125.6, 124.7, 121.2, 112.4. MS: (ESI^+); calculated*: m/z* 530.68; found: *m/z*: 529.2 $[M-H]^-$, 530.2 $[M]^+$, 531.2 $[M+H]^+$. IR: 1585, 1484, 1327, 1274, 1105, 754, 697, 654.

12: 4 (143 mg, 0.2 mmol) and Lawesson's reagent (80 mg, 0.2 mmol) were heated in toluene (120 mL) at 90–100 °C for 5–6 hrs. The reaction was protected from the light with aluminum foil and monitored by TLC (hexanes/DCM 1:1). The solvent was removed under reduced pressure and the residue purified by chromatography column over silica gel (eluent: hexanes/DCM 1 : 1) to afford brown solid **12** (83% yield).

^{1}H-NMR (500 MHz, $CDCl_3$): δ ppm 7.74 (d, 2H, J_3 = 7.7 Hz), 7.76 (s, 2H), 7.43 (d, 5H, J_3 = 8.2 Hz), 7.30–7.27 (m, 7H), 7.14–7.13 (m, 10H), 7.08–7.05 (m, 12H). ^{13}C-NMR (125 MHz, $CDCl_3$): δ ppm 223.8, 148.3, 147.5, 144.1, 143.7, 141.1, 131.2, 130.7, 129.5, 129.5, 128.0, 127.4, 126.4, 125.0, 124.8, 124.7, 124.6, 123.6, 123.1, 116.9. MS: (ESI^-); calculated*: m/z* 734.28; found: *m/z*: 734.2 $[M]^-$, 735.1 $[M+H]^-$. IR: 2923, 2854, 1588, 1496, 1323, 1269, 1216, 1097, 1028, 804, 757, 697, 669.

3.3 Barton's two fold coupling: general procedure for the synthesis of esters (13, 14, 15).

A solution of hydrazone **8** (295 mg, 3 eq, 1.2 mmol) was dissolved in 100 mL of anhydrous THF. Activated manganese oxide (100 mg, 10 eq, 12 mmol) was added to the solution and stirred at RT under N_2. The reaction was monitored by TLC using DCM as the eluent. The solution was filtered on celite and washing with dry THF to collect all the diaza-intermediate. The filtrate, without any further purification, was quickly added to 0.40 mmol (1 eq) of the corresponding thione **10, 11, 12**, and **13**. The reaction was stirred overnight at room temperature and covered with aluminum foil. The solvent was removed under reduced pressure, and the residue was purified by column chromatography.

14: the crude was purified by chromatography column over silica gel (eluent: hexanes/DCM 4 : 6), affording orange solid **14** (75% yield).

^{1}H-NMR (500 MHz, $CDCl_3$): δ ppm 8.55 (d, 1H, J_3 = 8.1 Hz), 8.43, (d, 1H, J_3 = 8.1 Hz), 8.37 (d, 1H, J_3 = 7.7 Hz), 8.23 (d, 1H, J_3 = 7.9 Hz), 8.19 (d, 1H, J_3 = 7.9 Hz), 7.60 (d, 3H, J_3 = 7.3 Hz), 7.35–7.31 (m, 3H), 7.25–7.18 (m, 4H), 4.05 (s, 3H); ^{13}C-NMR (125 MHz, $CDCl_3$): δ ppm 168.9, 141.7, 141.7, 141.6, 140.3, 140.1, 139.6, 139.1, 138.4, 138.3, 130.6, 129.7, 129.6, 129.5, 129.4, 127.6, 127.2, 127.2, 127.1, 127.0, 126.8, 126.5, 126.0, 124.8, 120.2, 120.1, 52.6. MS: (ESI$^+$); calculated*: m/z* 381.1; found: *m/z*: 409.1 [M+Na]$^+$; IR: 3059, 2924, 2856, 1718, 1604, 1445, 1262, 1190, 1137, 1088, 736.

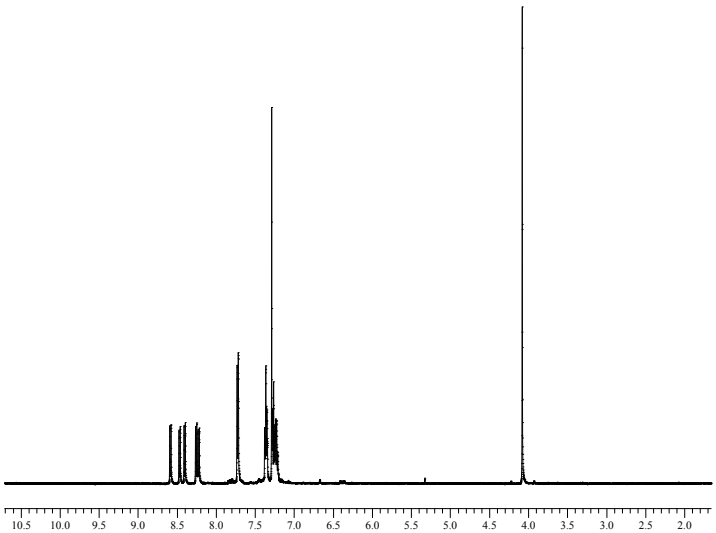

Figure S17. ^{1}H-NMR of compound **14.**

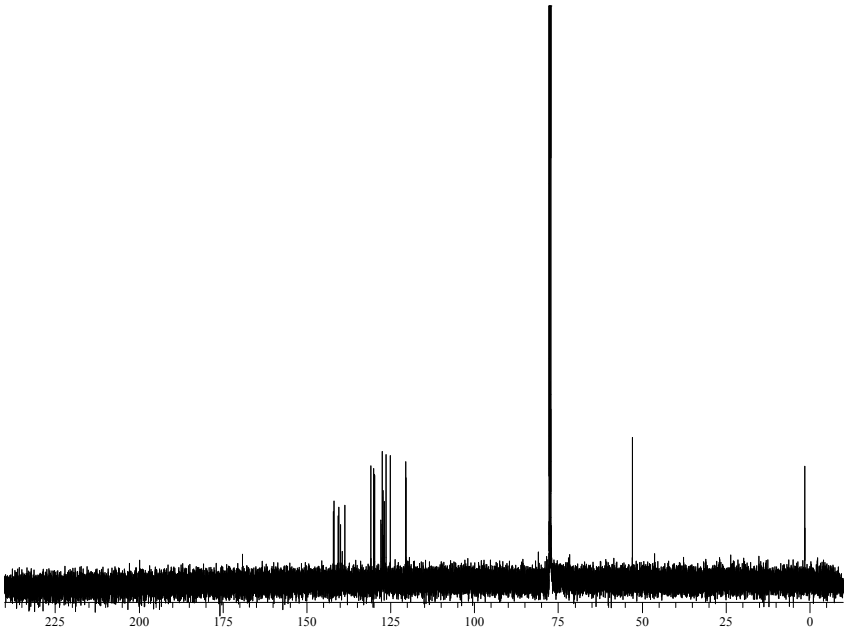

Figure S18. ^{13}C-NMR of compound **14.**

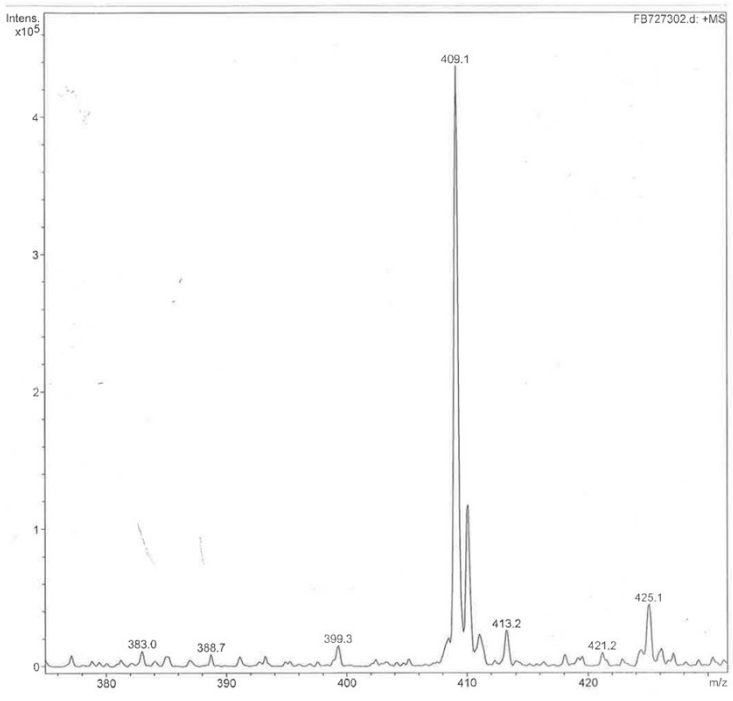

Figure S19. MS of compound **14.**

15: the crude was purified by chromatography column over silica gel (eluent: hexanes/DCM 6:4), affording red solid **15** (67% yield).

^{1}H-NMR (500 MHz, $CDCl_3$): δ ppm 8.52 (d, 1H, J_3 = 8.2 Hz), 8.39 (d, 1H, J_3 = 7.9 Hz), 8.22–8.20 (m, 2H), 8.06 (d, 1H, J_3 = 8.8 Hz), 7.66 (d, 1H, J_3 = 7.5 Hz), 7.31–7.27 (m, 11H including $CDCl_3$), 7.23 (q, 2H, J_3 = 7.7 Hz), 7.17–7.15 (m, 8H), 7.07 (t, 4H, J_3 = 7.7 Hz), 6.85–6.81 (m, 2H), 4.06 (s, 3H). ^{13}C-NMR (125 MHz, $CDCl_3$): δ ppm 169.1, 149.3, 149.2,147.4, 147.4, 142.7, 142.5, 141.1, 140.2, 139.3, 138.7, 138.6, 135.7, 133.1, 133.0, 129.5, 129.4, 129.2, 128.2, 128.2, 127.9, 127.2, 126.6, 126.0, 125.6, 125.0, 124.5, 123.7, 123.6, 122.1, 122.0, 114.6, 114.6, 52.48. MS: (ESI$^-$); calculated*: m/z* 720.28; found: *m/z*: 743.3 $[M+Na]^+$,744.3 $[M+H+Na]^+$; IR: 3062, 2923, 2855, 2258, 1726, 1589, 1488, 1447, 1329, 1271, 1129, 761, 695.

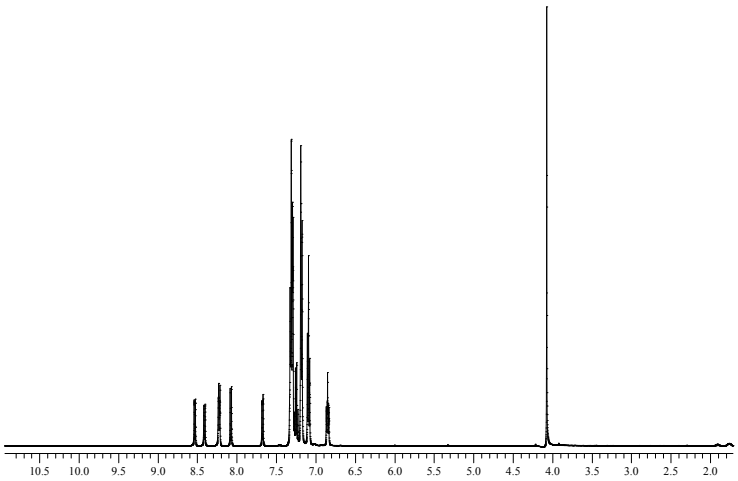

Figure S20. ^{1}H-NMR of compound **15.**

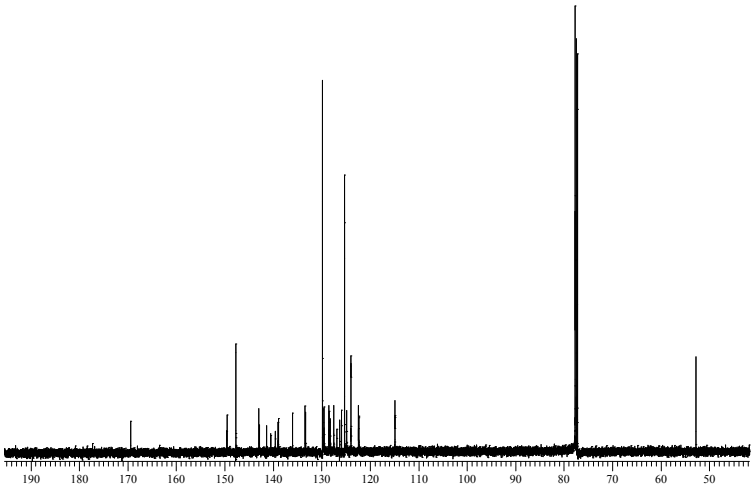

Figure S21. ^{13}C-NMR of compound **15.**

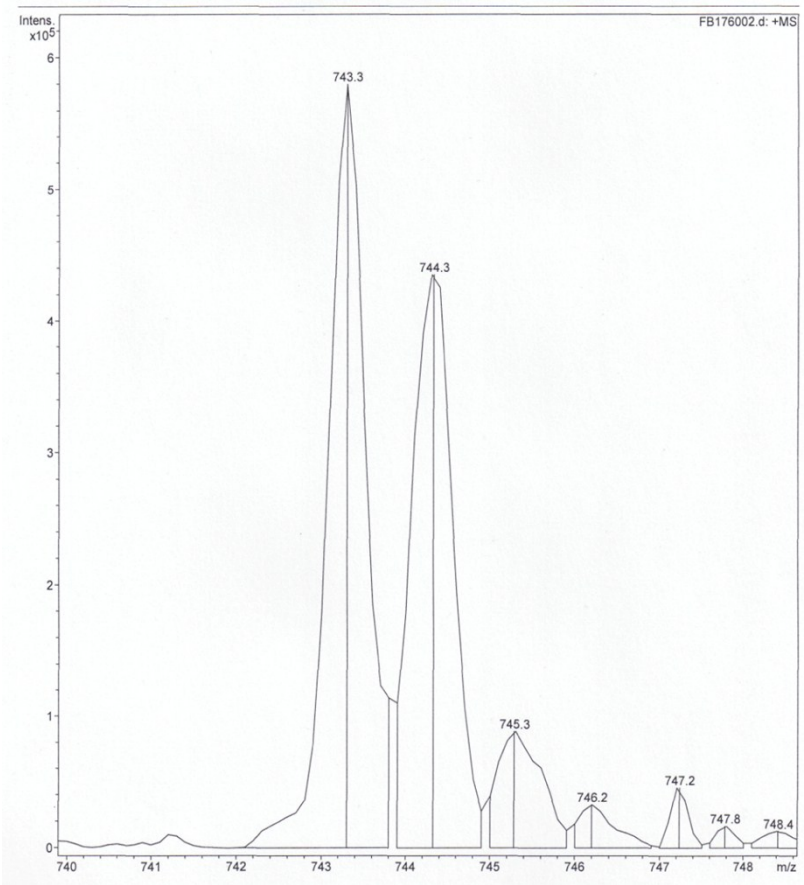

Figure S22. MS of compound **15.**

16: the crude was purified by chromatography column over silica gel (eluent: hexanes/DCM 1:1), affording dark solid **16** (50% yield).

^{1}H-NMR (500 MHz, $CDCl_3$): δ ppm 8.52 (d, 1H, J_3 = 7.5 Hz), 8.40 (d, 1H, J_3 = 7.8 Hz), 8.30 (d, 1H, J_3 = 8.3 Hz), 8.20 (d, 1H, J_3 = 8.0 Hz), 8.16 (d, 1H, J_3= 8.3 Hz), 7.87 (s, 2H), 7.68 (d, 1H, J_3 = 7.5 Hz), 7.44 (d, 4H, J_1 = 8.4 Hz), 7.35-7.21 (m, 13H including $CDCl_3$), 7.14–7.04 (m, 20H), 4.05 (s, 3H); ^{13}C-NMR (125 MHz, $CDCl_3$): δ ppm 168.9, 147.9, 147.9, 147.6, 142.0, 141.8, 141.2, 140.2, 139.4, 139.3, 139.2, 139.1, 139.0, 138.0, 137.9, 131.3, 131.3, 130.3, 129.6, 129.5, 129.4, 129.4, 129.1, 127.7, 127.5, 127.4, 127.2, 126.9, 126.9, 126.7, 126.4, 125.9, 125.5, 125.5, 124.8, 123.5, 123.4, 117.6, 117.6, 52.55. MS (Maldi-TOF); DCM/Ditranol; calculated*:* *m/z* 924.37; found *m/z*: 924.4 $[M]^+$, 925.4 $[M+H]^+$, 926.4 $[M+2H]^+$; IR: 3013, 2948, 2061, 1722, 1592, 1428, 1265, 1190, 1138, 1087, 751.

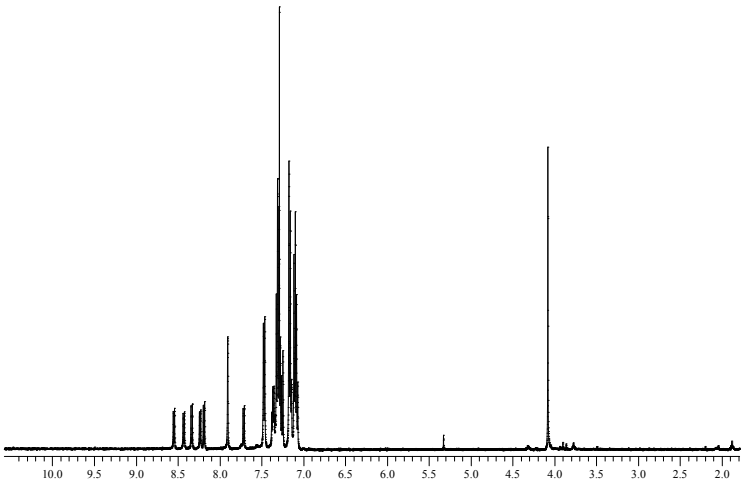

Figure S23. ^{1}H-NMR of compound **16.**

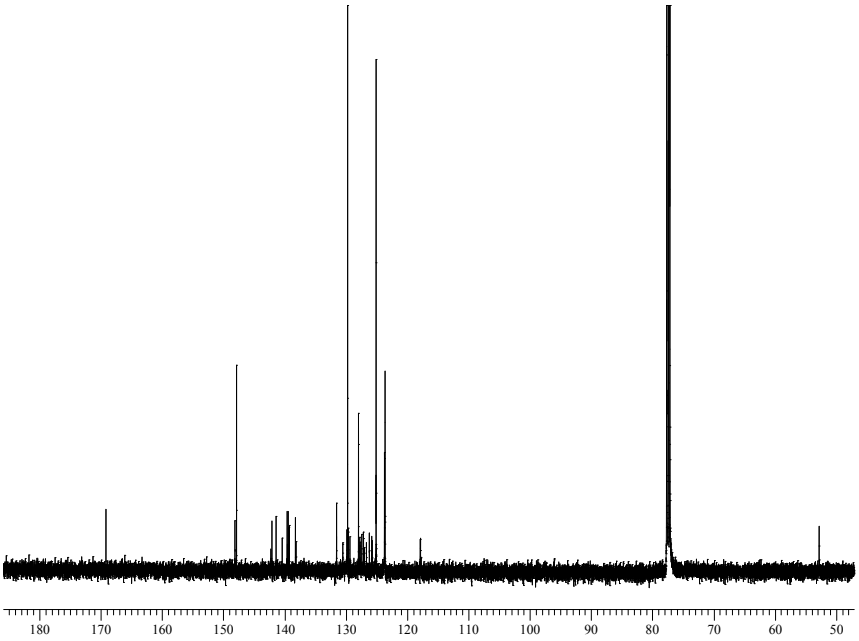

Figure S24. ^{13}C-NMR of compound **16.**

17: the crude was purified by chromatography column over silica gel (eluent: hexanes/DCM 1:1) affording red solid (54% yield).

^{1}H-NMR (300 MHz, $CDCl_3$): δ ppm 8.47 (dd, 1H, J_1 = 7.8 Hz, J_2 = 0.9Hz), 8.36 (dd, 1H, J_1 = 7.8 Hz, J_2 = 0.9Hz), 8.22 (t, 2H, J_1 = 8.7 Hz), 8.08 (d, 1H, J_1 = 8.7 Hz), 7.65 (dd, 1H, J_1 = 7.7 Hz, J_2 = 1.0 Hz), 7.30 (td, 1H, J_1 = 7.6 Hz, J_2 = 1.2 Hz), 7.26-7.13 (m, 4H), 6.75–6.70 (m, 2H), 4.05 (s, 3H), 3.92 (s, 3H), 3.91(s, 3H); ^{13}C-NMR (75 MHz, $CDCl_3$): δ ppm 169.0, 161.3, 161.3, 143.3, 143.2, 141.3, 140.2, 139.2, 138.8, 138.7, 135.6, 132.2, 132.1, 129.5, 129.2, 128.5, 128.3, 128.3, 127.2, 126.6, 125.9, 125.6, 124.6, 113.1, 105.3, 55.7, 52.5. MS: (ESI$^+$); calculated*: m/z* 446.15; found: *m/z*: 469.1[M+Na]$^+$; IR: 2927, 2844, 1722, 1607, 1489, 1461, 1433, 1295, 1239, 1202, 1167, 1131, 1031, 953, 765.

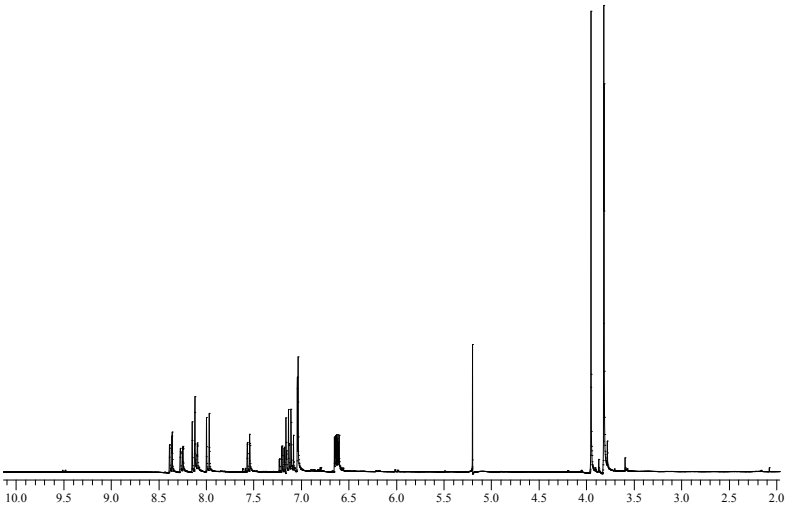

Figure S25. ^{1}H-NMR of compound **17.**

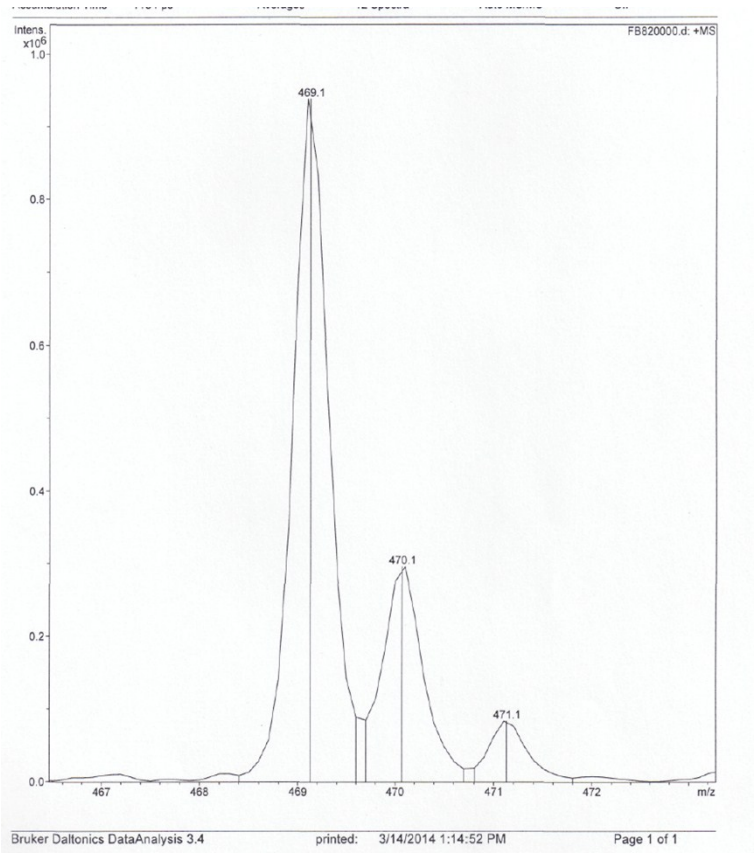

Figure S26. MS of compound **17.**

3.4 Hydrolysis of 9'9-fluorenylidene ester derivatives

BF1: **14** (0.18 mmol) was dissolved in CH_3CN (30 mL) and treated with LiOH (excess, 86.4 mg, 3.6 mmol) dissolved in water (10 mL). The reaction was stirred at RT for 5–6 hrs and monitored by TLC (eluent mixture: DCM : hexanes; 1 : 1). Acetonitrile was removed under reduced pressure and the crude was extracted with AcOEt (3 × 25 mL) and a 10% HCl water solution. The combined organic layers were dried over $MgSO_4$ and concentrated to dryness under reduced pressure affording orange solid **BF1** which was recrystallized from hot cyclohexane (75% yield).

^{1}H-NMR (500 MHz, *d6*-Acetone): δ ppm 8.60 (dd, 1H, J_1 = 7.9 Hz, J_2 = 0.9 Hz), 8.46 (d, 1H, J_1 = 7.5 Hz), 8.42 (d, 1H, J_1 = 7.7 Hz), 8.40 (d, 1H, J_1 = 8.1 Hz), 8.29 (d, 1H, J_1 = 7.9 Hz), 7.86 (d, 2H, J_1 = 7.5 Hz), 7.82 (d, 2H, J_1 = 7.6 Hz, J_2 = 0.9 Hz), 7.42–7.36 (m, 3H), 7.34–7.26 (m, 3H). ^{13}C-NMR (125 MHz, *d6*-Acetone): δ ppm 141.98, 139.9, 139.03, 131.10, 129.73, 127.94, 127.58, 127.36, 125.43, 120.61. MS: (ESI$^-$); calculated*: m/z* 372.12; found: *m/z*: 370.9 [M-H]$^-$; IR: 3067, 2924, 2857, 1697, 1438, 1342, 1279, 1151, 934, 764, 726.

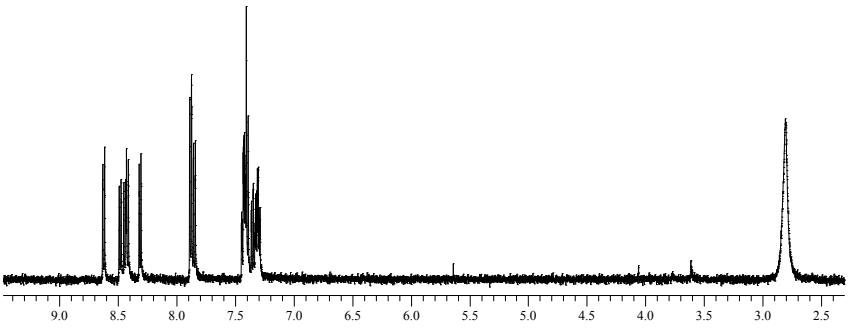

Figure S27. ^{1}H-NMR of compound **BF1.**

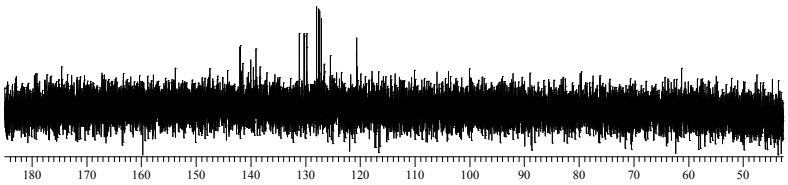

Figure S28. ^{13}C-NMR of compound **BF1.**

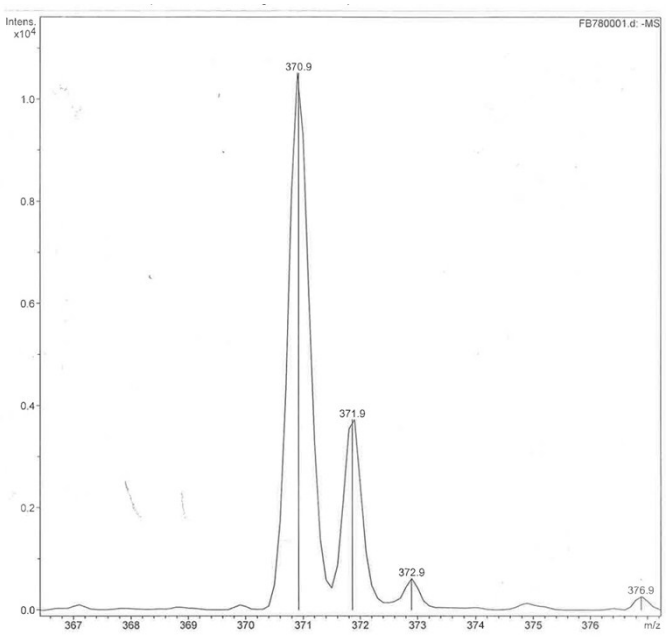

Figure S29. MS of compound **BF1.**

General procedure for BF3a, BF3b, and BF3d

The corresponding ester derivatives **15**, **16**, and **17** (0.20 mmol) were dissolved in 40 mL of a CH_3CN / methanol (1:1 v/v) solvent mixture and treated with an excess of NaOH (20–25 mL of a 3M water solution). The reaction was gently heated at 40–50 °C until no more ester was observed by TLC. Reaction time varies from 5 hrs to 12 hrs. Work up: acetonitrile and methanol were removed under reduced pressure and the crude was extracted with DCM (3 × 30 ml) and a 10% HCl solution. The organic layers were gathered, dried over Na_2SO_4 and evaporated under reduced pressure. The solid was washed with cyclohexane or pentane, yielding corresponding acids **BF3a**, **BF3b**, and **BF3d**.

BF3a: A dark violet solid was obtained by washing with hot pentane (yield 90%).

^{1}H-NMR (500 MHz, [D_6]DMSO): δ ppm 8.33 (d, 1H, J = 8.0 Hz), 8.25 (m, 2H), 8.12 (d, 1H, J = 8 Hz), 8.06 (d, 1H, J = 8 Hz), 7.55 (d, 1H, J = 8 Hz), 7.40–6.90 (m, 25H), 6.75 (m, 2H). ^{13}C-NMR (125 MHz, $CDCl_3$): δ ppm 170.1, 149.5, 146.9,146.4, 142.2, 140.05, 139.2, 138.7, 138.4, 136.9, 135.07, 132.3, 130.01, 129.22, 128.78, 128.42, 128.19, 127.6, 126.6, 126.16, 125.76, 125.25, 124.42, 121.60, 113.7.MS: (ESI$^-$); calculated*: m/z* 706.26; found: *m/z*: 705.3 [M-H]$^+$, 706.0 [M]$^+$; HR MS: (ESI$^+$); calculated*: m/z* 706.2620; found: *m/z*: 706.2648; IR: broad 3600-3400, 3030, 2924, 2857, 1694, 1589, 1487, 1320, 1272, 754, 695.

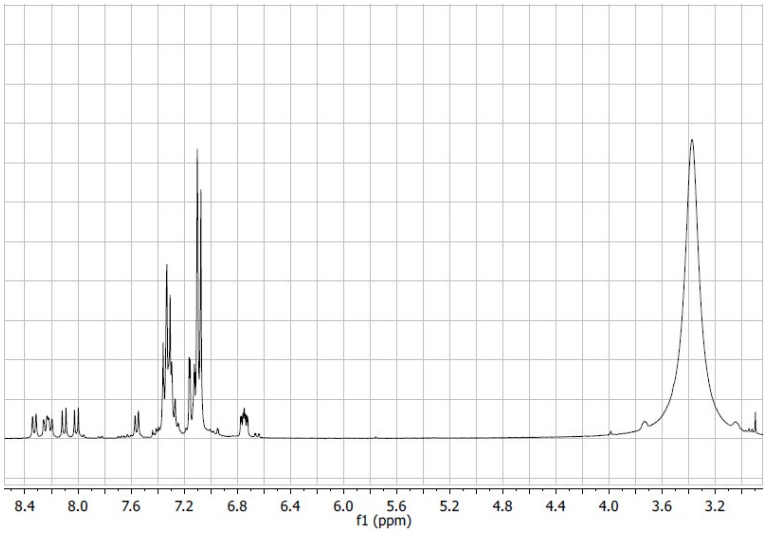

Figure S30. ^{1}H-NMR of compound **BF3a.**

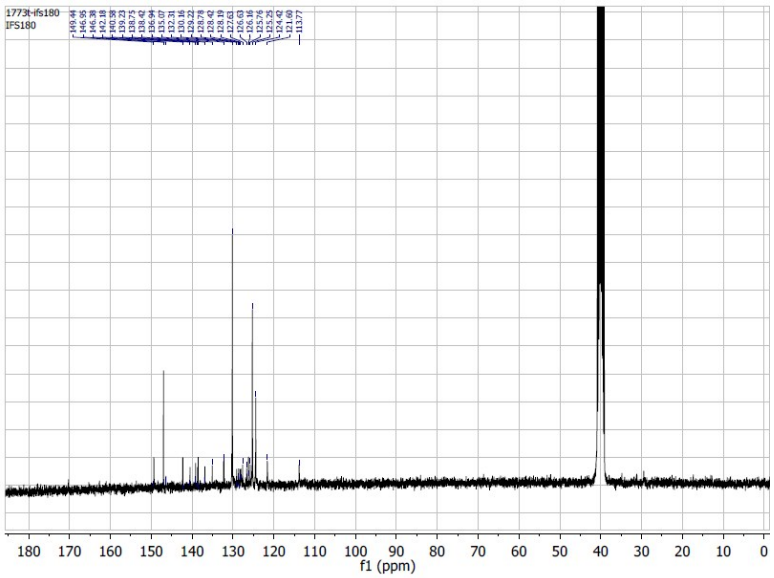

Figure S31. ^{13}C-NMR of compound **BF3a.**

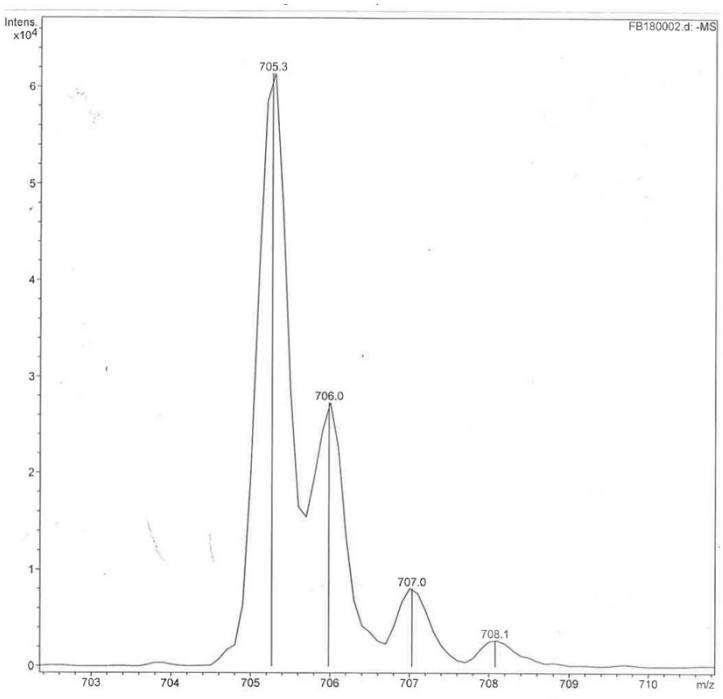

Figure S32. MS of compound **BF3a.**

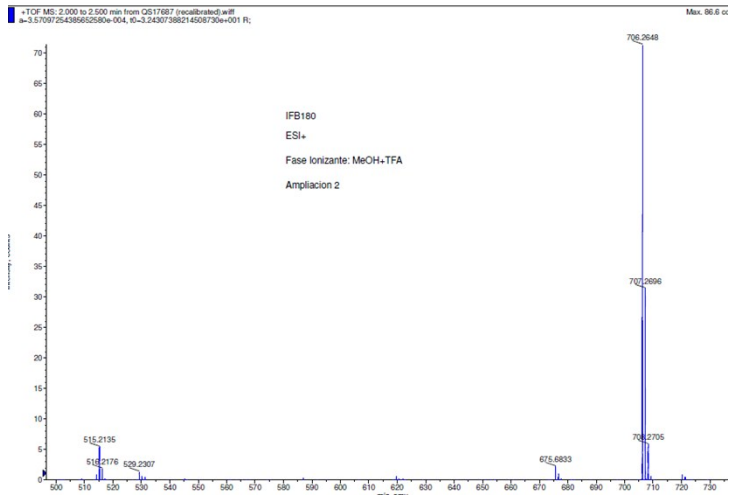

Figure S33. HR MS of compound **BF3a.**

BF3b: A dark solid was obtained by washing with hot pentane (yield 42%).

^{1}H-NMR (500 MHz, [D_6]DMSO): δ ppm 8.40–8.10 (m, 5H), 7.6–6.9 (m, 32 H). ^{13}C-NMR (125 MHz, $CDCl_3$): δ ppm 147.6, 147.3, 131.4, 130.1, 128.3, 124.85, 123.9, 123.26. MS: (ESI^-); calculated*: m/z* 909.08; found: *m/z*: 909.1 $[M]^+$; HR MS: (ESI^+); calculated*: m/z* 908.3403; found: *m/z*: 908.3403 $[M+H]^+$; IR: broad 3400, 2924, 2856, 1714, 1650, 1497, 1280, 752, 696.

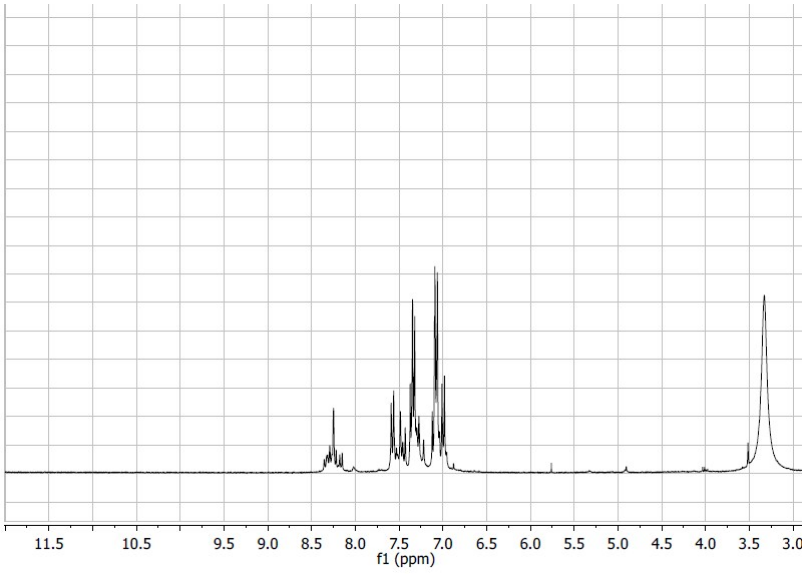

Figure S34. ^{1}H-NMR of compound **BF3b.**

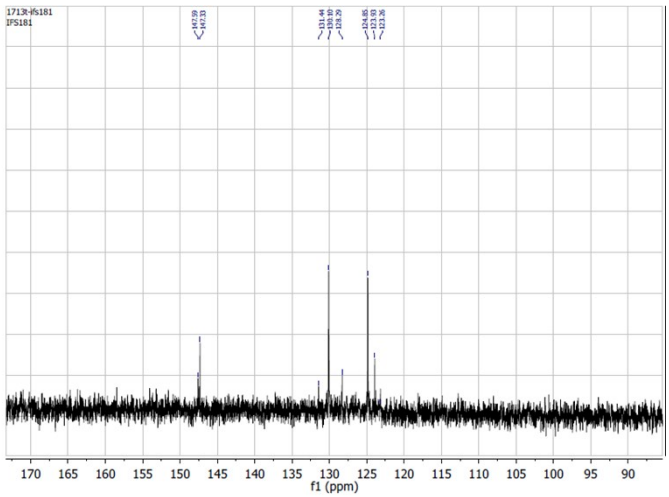

Figure S35. ^{13}C-NMR of compound **BF3b.**

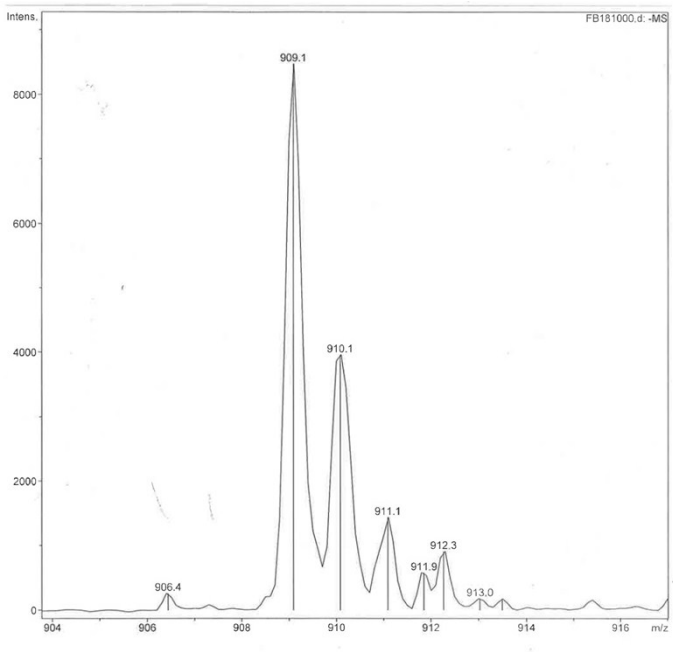

Figure S36. MS of compound **BF3b.**

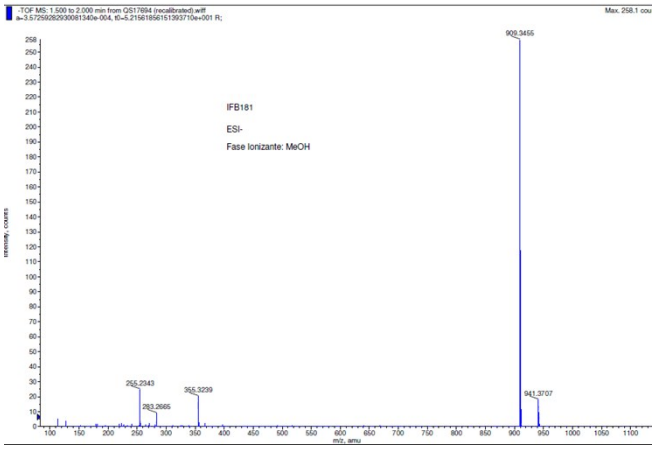

Figure S37. HR MS of compound **BF3b.**

BF3c: A red solid was obtained by washing with hot cyclohexane (yield 95%).

^{1}H-NMR (500 MHz, d_6-Acetone): δ ppm 8.53 (d, 1H, J_1 = 7.7 Hz), 8.39 (d, 1H, J_1 = 7.7 Hz), 8.25 (d, 1H, J_1 = 8.8 Hz), 8.15 (d, 1H, J_1 = 8.8 Hz), 7.78. (d, 1H, J_1 = 7.7 Hz), 7.46 (d, 2H, J_1 = 2.7 Hz), 7.39–7.28 (m, 4H), 6.86–6.83 (m, 2H), 3.95 (s, 6H); ^{13}C-NMR (125 MHz, d_6-Acetone): δ ppm 169.6, 162.7, 162.6, 144.4, 144.3, 142.2, 140.7, 139.8, 139.7, 139.2, 135.8, 132.4, 132.3, 130.5, 129.7, 129.2, 129.0, 128.9, 128.2, 128.1, 126.7, 126.5, 125.8, 114.3, 106.4, 106.4, 56.1. MS: (ESI$^-$); calculated*: m/z* 432.14; found: *m/z*: 430.9 [M-H]$^+$, 431.9 [M]$^+$; HR MS: (ESI^{-+}); calculated*: m/z* 432.1362; found: *m/z*: 433.1417 [M+H]$^+$; IR: 3416, 2925, 2854, 1604, 1461, 1401, 1300, 1236, 1030, 765.

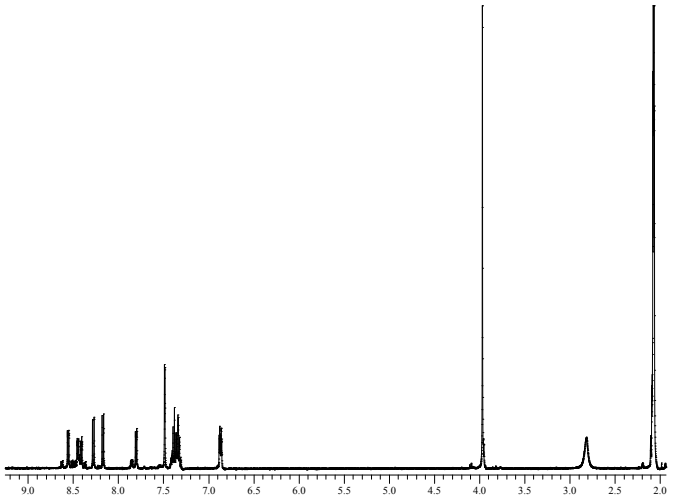

Figure S38. ^{1}H-NMR of compound **BF3c.**

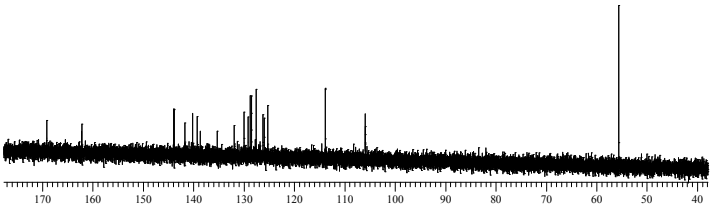

Figure S39. ^{13}C-NMR of compound **BF3c.**

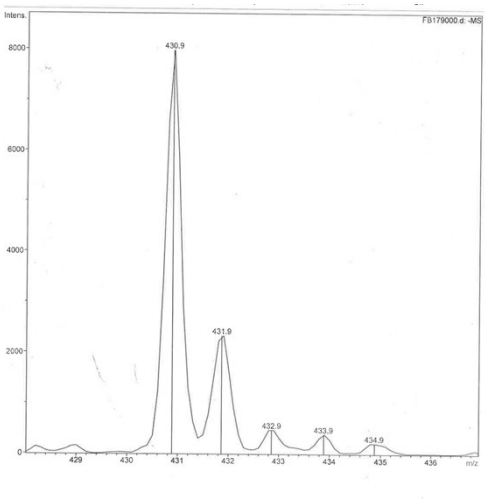

Figure S40. MS of compound **BF3c.**

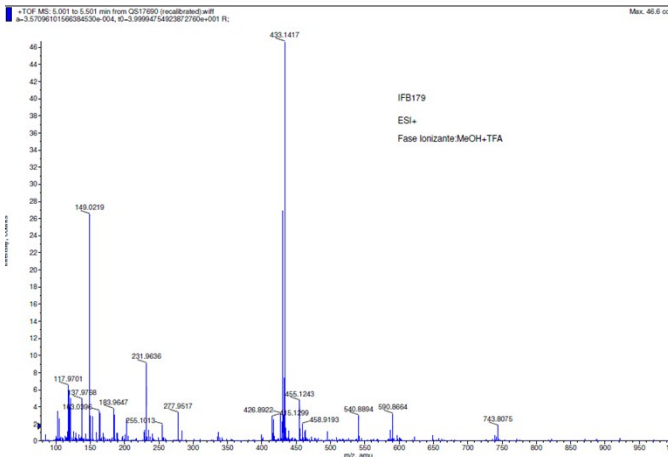

Figure S41. HR MS of compound **BF3c.**

Theoretical calculations

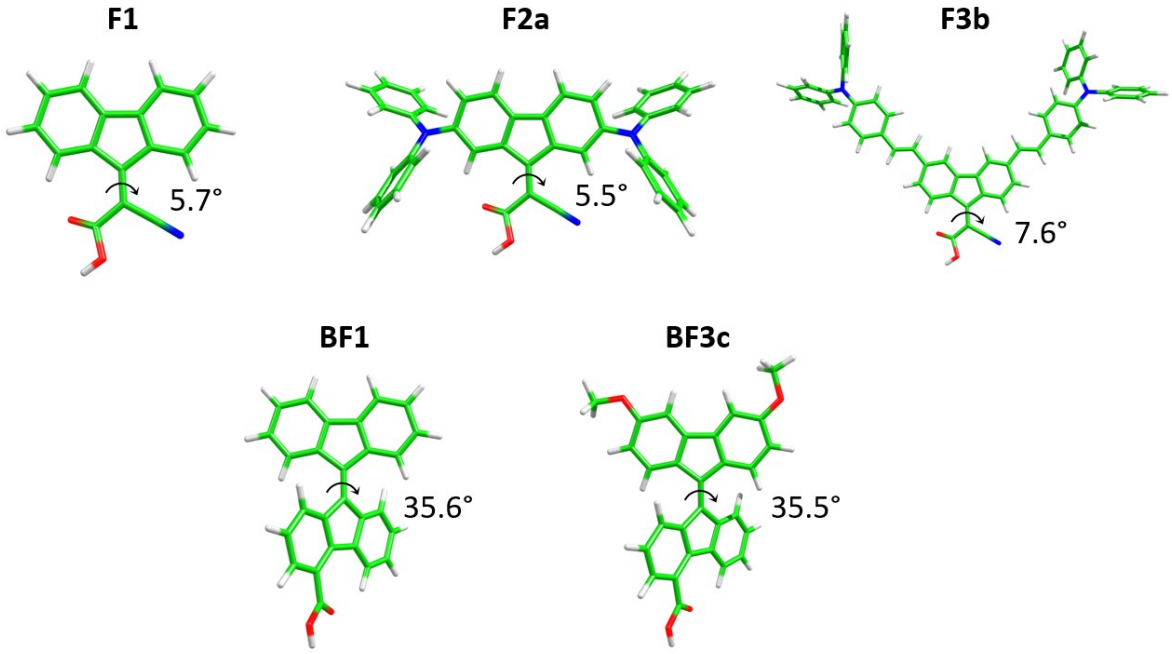

Figure S42. B3LYP/cc-pVDZ-optimized geometries calculated for **F1**, **F2a**, **F3b**, **BF1** and **BF3c** in dichloromethane. The rotational angle between the fluorene unit and the acceptor cyanoacrylic acid group in **F1**, **F2a** and **F3b** and between the two fluorene units in **BF1** and **BF3c** are indicated.

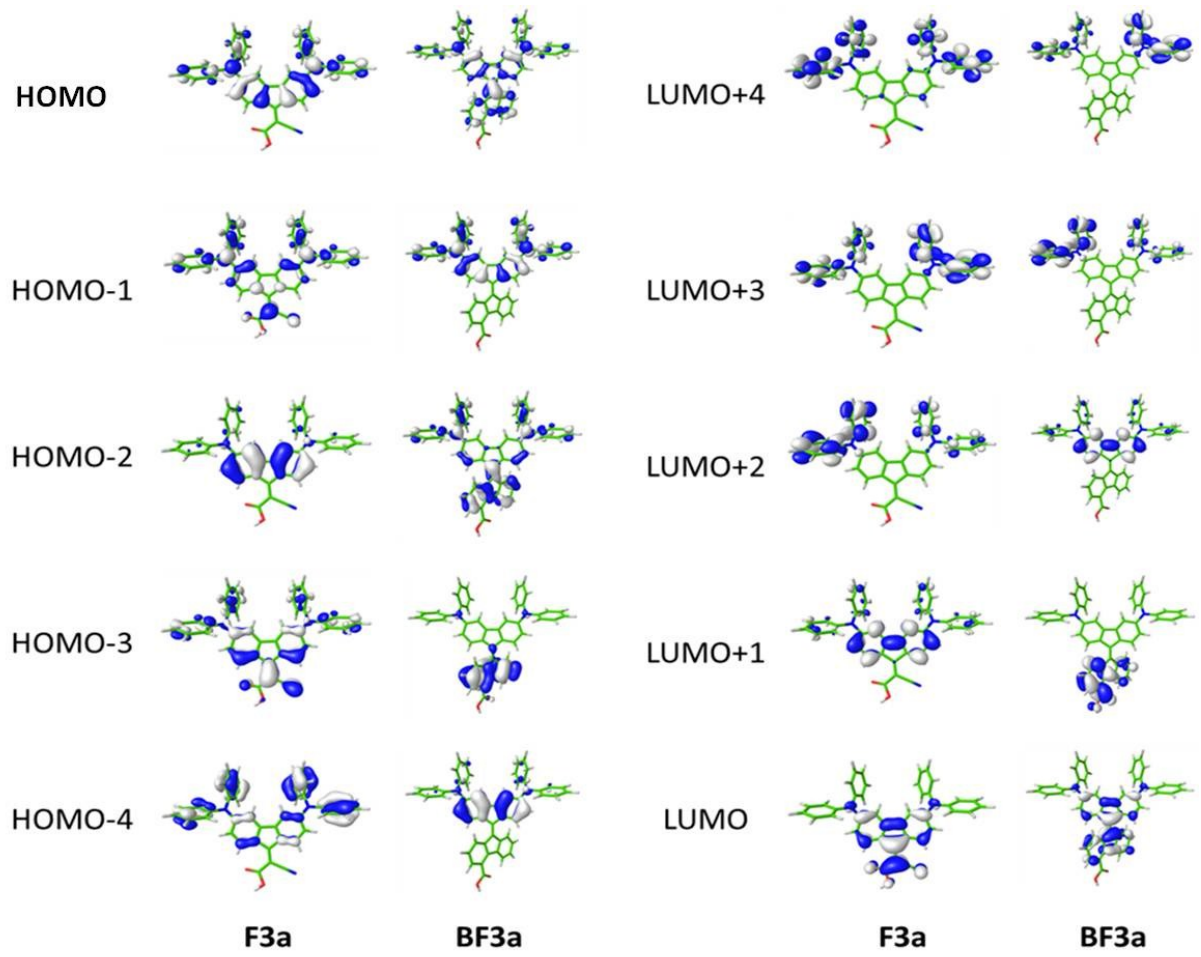

Figure S43. Energy diagram showing the isovalue contours (±0.03 a.u.) computed for the HOMOs and LUMOs of the representative dyes **F3a** and **BF3a** at the B3LYP/cc-pVDZ level.

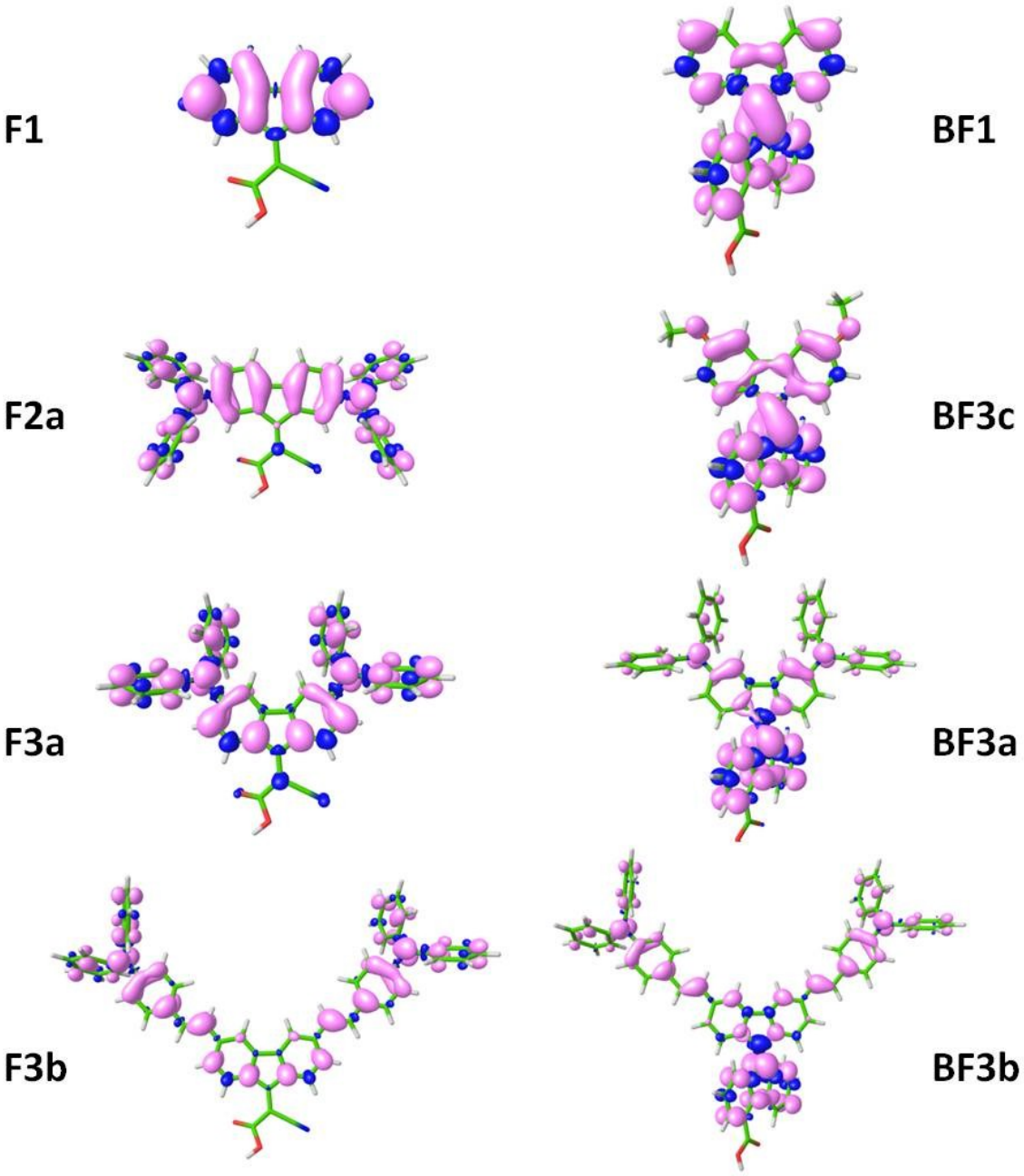

Figure S44. Representation of the electron spin densities calculated for the optimized cationic species at the B3LYP/cc-pVDZ level in dichloromethane.

Table S1. Lowest-energy singlet excited states calculated for all the investigated dyes using the TD-DFT approach and dimethylformamide as solvent. Vertical excitation energies (*E*), oscillator strengths (*f*), dominant monoexcitations with contributions (within parentheses) greater than 40%, and description of the excited state are summarized. H and L denote HOMO and LUMO, respectively.

Dye	State	*E* (eV)	*E* (nm)	*f*	Monoexcitations	%	Description
F1	S_1	2.4298	510	0.0011	H→L	99	CT
	S_2	3.4695	357	0.2864	H-1→L	56	Core+Acceptor
					H-2→L	40	CT
	S_3	3.4942	355	0.2460	H-2→L	54	CT
					H-1→L	41	Core+Acceptor
	S_6	4.7593	261	0.7128	H→L+1	88	Core
F2a	S_1	1.3353	929	0.0358	H→L	99	CT
	S_2	1.9617	632	0.0010	H-1→L	100	CT
	S_4	3.1407	395	0.6063	H→L+1	86	Donor
	S_6	3.3876	366	0.3764	H-5→L	71	CT
F3a	S_1	1.9131	648	0.2640	H→L	97	CT
	S_2	2.3720	523	0.5242	H-1→L	99	CT
	S_3	2.8377	437	0.1263	H-2→L	95	CT
	S_4	3.4358	361	0.1901	H→L+1	87	Core+Donor
	S_5	3.5959	345	0.1260	H-3→L	82	Core+Acceptor
F3b	S_1	1.6024	774	0.6920	H→L	97	CT
	S_2	1.8065	686	0.4811	H-1→L	100	CT
	S_3	2.3299	532	0.0019	H-2→L	88	CT
	S_4	2.8114	441	0.4643	H-3→L	98	Core+Acceptor
	S_5	2.8788	431	0.5799	H-4→L	80	CT
	S_6	3.0389	408	0.6747	H→L+1	95	Donor
	S_7	3.0859	402	0.4811	H-1→L+1	83	Donor
BF1	S_1	2.4411	508	0.5841	H→L	100	Core
	S_4	3.2820	378	0.0342	H→L+1	98	CT
	S_5	3.4961	355	0.0301	H-3→L	89	Core
	S_6	3.5928	345	0.0322	H-4→L	76	Core
BF3a	S_1	1.9397	639	0.1989	H-1→L	98	CT
	S_2	1.9915	623	0.8444	H→L	100	Core
	S_5	2.8564	434	0.0715	H-4→L	89	CT
	S_6	2.8929	429	0.0789	H-2→L	85	Core
	S_9	3.4297	362	0.1644	H-1→L+2	90	Donor
BF3b	S_1	1.7215	720	0.5113	H-1→L	97	CT
	S_2	1.7784	697	0.8792	H→L	100	CT
	S_3	2.3332	531	0.3243	H-2→L	99	Core
	S_7	2.9242	424	1.2990	H→L+2	77	Donor
	S_{10}	3.0581	405	0.5816	H-1→L+2	88	Donor
BF3c	S_1	2.3526	527	0.7128	H→L	100	Core
	S_4	3.0643	405	0.0342	H→L+1	98	CT
	S_5	3.3389	371	0.0733	H-3→L	92	Core

Table S2. Lowest-energy doublet excited states calculated for the cationic species of representative dyes using the TD-DFT approach. Vertical excitation energies (*E*), oscillator strengths (*f*), dominant monoexcitations with contributions (within parentheses) greater than 40%, and description of the excited state are summarized. H and L denote HOMO and LUMO, respectively.

Cation	State	*E* (eV)	*E* (nm)	*f*	Monoexcitations	%	Description
F2a	D_1	0.9877	1255	0.487	H-1→SOMO	94	Donor
	D_2	1.4480	856	0.1327	SOMO→L	92	CT
	D_9	2.2179	559	0.0116	H-6→SOMO	50	Donor
F3a	D_1	0.3793	3269	0.0835	H-1→SOMO	98*	Donor
	D_2	1.2310	1007	0.0234	H-2→SOMO	94	Donor
	D_3	1.5924	779	0.1314	H-3→SOMO	91	Donor
	D_4	1.6050	773	0.015	H-1→L	59	CT
	D_5	1.8024	688	0.0042	H-4→SOMO	97	Donor
	D_6	1.8328	676	0.014	H-5→SOMO	98	Donor
	D_7	1.9492	636	0.0099	H-6→SOMO	93	Donor
	D_{13}	2.2058	562	0.1298	SOMO→L	85	Donor
F3b	D_1	0.3112	3984	0.2207	H-1→SOMO	99*	Donor
	D_2	1.0220	1213	0.1204	H-2→SOMO	94	Donor
	D_3	1.1725	1057	0.2727	H-3→SOMO	98	Donor
	D_4	1.4159	876	0.0098	H-1→L	61	CT
	D_5	1.4996	827	0.0557	H-4→SOMO	88	Donor
	D_6	1.7759	698	0.2864	SOMO→L	65	CT
	D_{11}	2.0456	606	0.2581	H-7→SOMO	40	Donor
BF3a	D_1	0.5362	2312	0.0639	H-1→SOMO	94	CT
	D_4	1.4711	843	0.0234	H-1→L	64	CT
	D_5	1.6480	752	0.0998	H-4→SOMO	61	CT
	D_6	1.6530	750	0.4312	SOMO→L	40	Core
	D_7	1.8555	668	0.2588	H-1→L	55	CT
	D_8	2.0833	595	0.0224	H-7→SOMO	47	Donor
BF3b	D_1	0.3218	3853	0.2014	H-1→SOMO	98*	Donor
	D_2	0.7906	1568	0.1911	H-2→SOMO	87	Donor
	D_3	1.1308	1096	0.1569	H-3→SOMO	94	Donor
	D_6	1.3178	941	0.4011	SOMO→L	42	CT
	D_7	1.5648	792	0.6233	H-1→L	57	CT
	D_{10}	1.8069	686	0.1614	H-5→SOMO	45	Donor
	D_{19}	2.2500	551	0.1745	H-2→L	44	Core

Photophysical measurements

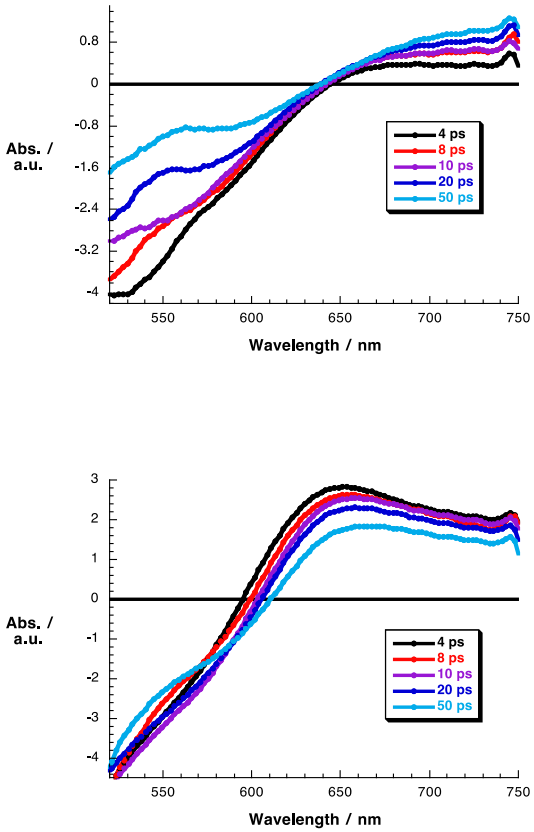

Figure S45. Differential absorption spectra obtained upon femtosecond flash photolysis (λ_{exc} = 480 nm) of 3 µm-thick TiO_2 films sensitized with **BF3a** (top) and **BF3b** (bottom) with several time delays at room temperature showing the spectral characteristics of the oxidized states generated after charge injection into TiO_2.

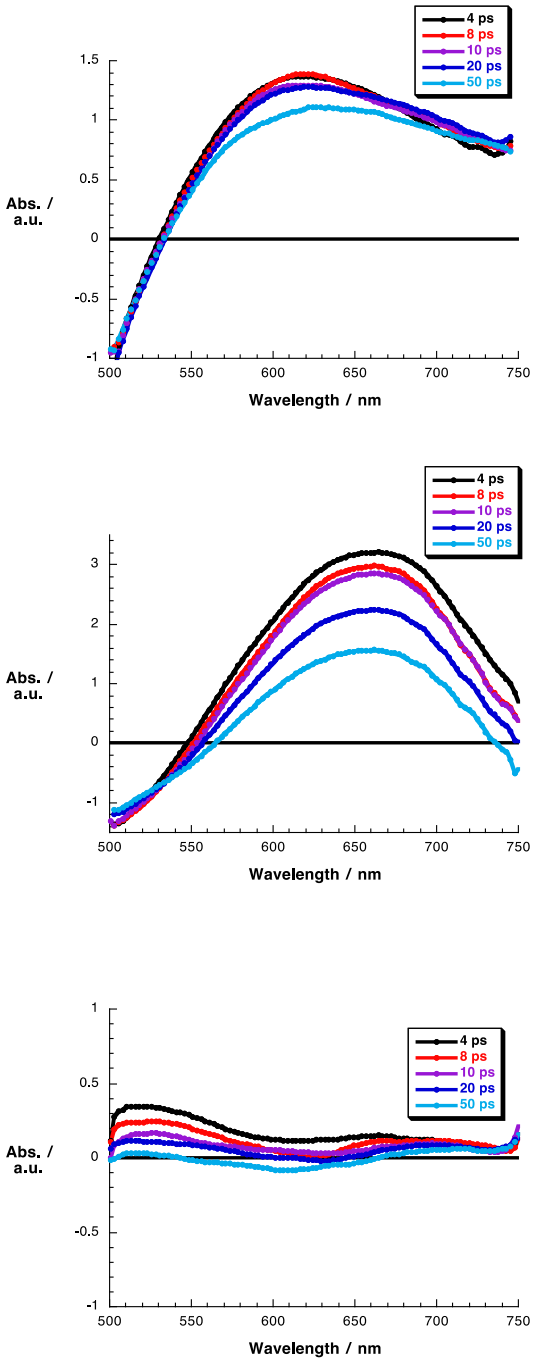

Figure S46. Differential absorption spectra obtained upon femtosecond flash photolysis (λ_{exc} = 480 nm) of 3 µm-thick TiO_2 films sensitized with **F2a** (top), **F3b** (middle) and **F3a** (bottom) with several time delays at room temperature showing the spectral characteristics of the oxidized states generated after charge injection into TiO_2.

Photovoltaic measurements

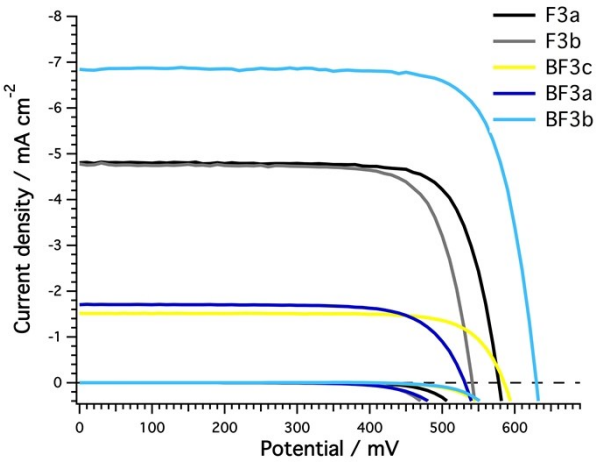

Figure S47. Photocurrent density-voltage characteristic curves of devices sensitized with **F3a**, **F3b**, **BF3a**, **BF3b** and **BF3c** measured under AM 1.5G simulated sunlight illumination (100 mW cm^{-2}) and in dark with different dyes.

Table S3. Detailed photovoltaic parameters of devices measured under AM 1.5G simulated sunlight illumination (100 mW cm^{-2}).

Dye	J_{sc} / mA cm^{-2}	V_{oc} / mV	FF	PCE / %
F3a	4.802	577	0.767	2.11
F3b	4.777	540	0.758	1.94
BF3a	1.702	530	0.738	0.66
BF3b	6.840	629	0.772	3.29
BF3c	1.514	584	0.766	0.67

1 H. Le Moal, R. Carrie, A. Foucaud, R. Danion-Bougot and C. Gadreau, *Bull. Soc. Chim. France*, 1968, **5**, 2156.

2 J. Ipaktschi and Sharifi, *Monatsh. Chem.*, 1998, **129**, 915.

3 Z. Wu, Y. Xiong, J. Zou, L. Wang, J. Liu, Q. Chen, W. Yang, J. Peng and Y. Cao, *Adv. Mater.,* 2008, **20**, 2359.

4 E. Preis, C. Widling, U. Scherf, S. Patil, G. Brunklaus, J. Schmidt and A. Thomas, *Polym. Chem.*, 2011, **2**, 2186.

5 S. Scheibye, R. Shabana, S.-O. Lawesson and C. Roemming, *Tetrahedron*, 1982, **38**, 993.

6 F. G. Brunetti, A. Varotto, N. A. Batara and F. Wudl, *Chem. Eur. J.*, 2011, **17**, 8604.